Monthly Notices
of the
ROYAL ASTRONOMICAL SOCIETY

MNRAS **478,** 3335–3355 (2018)
Advance Access publication 2018 April 28

doi:10.1093/mnras/sty1045

Galaxies in the act of quenching star formation

Salvatore Quai,[1,2]★ Lucia Pozzetti,[2] Annalisa Citro,[1,2] Michele Moresco[1,2] and Andrea Cimatti[1,3]

[1]*Dipartimento di Fisica e Astronomia, Università di Bologna, Via Gobetti 93/2, I-40129, Bologna, Italy*
[2]*INAF – Osservatorio Astronomico di Bologna, Via Gobetti 93/3, I-40129, Bologna, Italy*
[3]*INAF – Osservatorio Astrofisico di Arcetri, Largo E. Fermi 5, I-50125, Firenze, Italy*

Accepted 2018 April 20. Received 2018 March 26; in original form 2017 November 19

ABSTRACT

Detecting galaxies when their star formation is being quenched is crucial to understand the mechanisms driving their evolution. We identify for the first time a sample of quenching galaxies selected just after the interruption of their star formation by exploiting the [O III] λ5007/H α ratio and searching for galaxies with undetected [O III]. Using a sample of ∼174000 star-forming galaxies extracted from the SDSS-DR8 at $0.04 \leq z < 0.21$, weidentify the ∼300 quenching galaxy best candidates with low [O III]/H α, out of ∼26000 galaxies without [O III] emission. They have masses between $10^{9.7}$ and $10^{10.8}$ $M_{\odot}$, consistently with the corresponding growth of the quiescent population at these redshifts. Their main properties (i.e. star-formation rate, colours, and metallicities) are comparable to those of the star-forming population, coherently with the hypothesis of recent quenching, but preferably reside in higher-density environments. Most candidates have morphologies similar to star-forming galaxies, suggesting that no morphological transformation has occurred yet. From a survival analysis we find a low fraction of candidates (∼0.58 per cent of the star-forming population), leading to a short quenching time-scale of $t_Q \sim 50$ Myr and an *e*-folding time for the quenching history of $\tau_Q \sim 90$ Myr, and their upper limits of $t_Q < 0.76$ Gyr and $\tau_Q < 1.5$ Gyr, assuming as quenching galaxies 50 per cent of objects without [O III] (∼7.5 per cent). Ourresults are compatible with a 'rapid' quenching scenario of satellites galaxies due to the final phase of strangulation or ram-pressure stripping. This approach represents a robust alternative to methods used so far to select quenched galaxies (e.g. colours, specific star-formation rate, or post-starburst spectra).

Key words: H II regions – ISM: lines and bands – galaxies: abundances – galaxies: evolution – galaxies: general.

1 INTRODUCTION

Since the pioneering work of Hubble (Hubble 1926), galaxies have been divided into two broad populations: blue star-forming (SF) spirals (late-type galaxies) and red ellipticals and lenticulars (early-type galaxies) with weak or absent star formation. The advent of massive surveys, such as the Sloan Digital Sky Survey (SDSS; York et al. 2000; Strauss et al. 2002), provided very large samples of all galaxy types and allowed to study their general properties with unprecedented statistics.

At low redshifts ($z \sim 0.1$), galaxies show a bimodal distribution of their colours (Strateva et al. 2001; Blanton et al. 2003; Hogg et al. 2003; Baldry et al. 2004; Balogh et al. 2004) and structural properties (Kauffmann et al. 2003; Bell et al. 2012). In a colour-magnitude diagram (CMD) or in a colour-mass diagram, early-type and bulge-dominated galaxies occupy a tight 'red sequence'. Instead, late-type, disc-dominated systems are spread in the so-called 'blue cloud' region. At higher redshifts, this bimodality has been clearly observed up to at least $z \sim 2$ (e.g. Cucciati et al. 2006; Willmer et al. 2006; Cirasuolo et al. 2007; Cassata et al. 2008; Kriek et al. 2008; Brammer et al. 2009; Williams et al. 2009; Muzzin et al. 2013). The increase of the number density and the stellar mass growth of the red population from $z \sim 1-2$ to the present (e.g. Bell et al. 2004; Blanton 2006; Bundy et al. 2006; Faber et al. 2007; Mortlock et al. 2011; Ilbert et al. 2013; Moustakas et al. 2013) suggests that a fraction of blue galaxies migrates from the blue cloud to the red sequence, together with a transformation of their morphologies and the suppression of the star formation (quenching) (e.g. Peng et al. 2010; Pozzetti et al. 2010). An interesting possibility is that both galaxy bimodality and the growth of the red population with cosmic time are due to a migration of the disc-dominated galaxies from the blue cloud to the red sequence when they experience the interruption (quenching) of the star formation while, at the same time, there

★ E-mail: salvatore.quai@unibo.it

is a continued assembly of massive (near L∗), red spheroidal galaxies through dry merging along the red sequence (Faber et al. 2007; Ilbert et al. 2013). It is also thought that these transitional scenarios depend on the environment where galaxies are located (e.g. Goto et al. 2003; Balogh et al. 2004; Peng et al. 2010).

Interestingly, the CMD region between the blue and red populations is underpopulated (e.g. Balogh et al. 2004). In particular, the distribution of optical colours, at fixed magnitude, can be fitted by the sum of two separate Gaussian distributions (Baldry et al. 2004), without the need for an intermediate galaxy population. This suggests that the transition time-scale from SF to passive galaxies must be rather short (e.g. Martin et al. 2007; Mendez et al. 2011; Mendel et al. 2013; Salim 2014). By considering also ultraviolet data, it has been possible to better explore the CMD at $z\sim 0.1$, thanks to colours more sensitive to young stellar populations (lifetimes $<$100 Myr) with respect to the standard optical CMD (Martin et al. 2007; Salim et al. 2007; Schiminovich et al. 2007; Wyder et al. 2007). This showed that there is an excess of galaxies in a wide region between the red sequence and the blue cloud that is not easily explained with a simple superposition of the two populations. This intermediate region has been named 'green valley' and it should be populated by galaxies just in the process of interrupting their star formation (quenching).

The physical origin of the star formation quenching is still unclear, and many mechanisms have been proposed (see Somerville & Davé 2015). The most appealing options include (i) the radiative and mechanical processes due to active galactic nucleus (AGN) activity (e.g. Fabian 2012), (ii) the quenching due to the gravitational energy of cosmological gas accretion delivered to the inner-halo hot gas by cold flows via ram-pressure drag and local shocks (*gravitational quenching*; Dekel & Birnboim 2008), the suppression of star formation when a disc becomes stable against fragmentation to bound clumps without requiring gas consumption, the removal or termination of gas supply (*morphological quenching*; Martig et al. 2009), and the processes due to the interaction between the galaxy gas with the intracluster medium in high-density environments (*environmental or satellite quenching*; Gunn & Gott 1972; Larson, Tinsley & Caldwell 1980; Moore et al. 1998; Balogh, Navarro & Morris 2000; Bekki 2009; Peng et al. 2010, 2012). The quenching processes are also termed internal or environmental, depending on whether they are originated within a galaxy or if they are triggered by the influence of the environment (e.g. the intracluster medium). These processes are not mutually exclusive, and they could in principle take place together on different time-scales. For instance, the environmental quenching (e.g. gas stripping) is expected to be dominant only in dense groups and clusters. The internal AGN feedback and gravitational heating quenching are thought to be limited to haloes with masses higher than 10^{12} $M_{\odot}$, whereas morphological quenching can play an important role also in less massive haloes and in field galaxies.

Despite the importance and necessity of quenching, the actual identification of galaxies where the suppression of the star formation is taking place remains very challenging. Several approaches have been exploited so far to find galaxies in the quenching phase. In particular, most studies focused on galaxies migrating from the blue cloud to the red sequence. For instance, green valley galaxies show varied morphologies (Schawinski et al. 2010), with a predominance of bulge-dominated disc shapes (Salim 2014). Furthermore, there is a consensus in interpreting the decreasing of the specific star formation rate (sSFR) with redder colours (e.g. Salim et al. 2007, 2009; Schawinski et al. 2014) as an indicator of recent quenching or rapid decrease of the star formation. However, Schawinski et al. (2014) argue that, despite the lower sSFR, the green valley is constituted by a superposition of two populations that share the same intermediate optical colours: the green tail of the blue late-type galaxies with no sign of rapid transition towards the red sequence (quenching time-scale of several Gyr) and a small population of blue early-type galaxies which are quickly transiting across the green valley (time-scale $\sim$1 Gyr) as a result of major mergers of late-type galaxies. The connection between quenching, red sequence, and mergers has been investigated by studying the so-called post-starburst (E+A or K+A) galaxies. These galaxies have morphological disturbances associated with gas-rich mergers and are spectroscopically characterized by strong Balmer absorptions (i.e. dominated by A type stars), although they do not show emission lines due to ongoing star formation (e.g. Poggianti et al. 2004, 2008; Quintero et al. 2004; Goto 2005). The strong Balmer absorption of post-starburst galaxies suggests that their star formation terminated 0.5–1Gyrago. Other interesting cases are represented by early-type galaxies with recently quenched blue stellar populations, or where star formation is occurring at low level and likely going to terminate soon (e.g. Kaviraj 2010; Thomas et al. 2010; McIntosh et al. 2014). Some recent results suggest that quenching may also occur with longer time-scales during the inside-out evolution of discs and the formation of massive bulges via secular evolution (e.g. Tacchella et al. 2015; Belfiore et al. 2017), or through the so-called strangulation process (Peng, Maiolino & Cochrane 2015). In addition to normal galaxies, many studies have been focused on systems hosting AGN activity in order to understand whether the released radiative and/or mechanical energy is sufficient to suppress star formation (e.g. Fabian 2012). Several results indicate that AGN feedback can indeed play a key role in the rapid quenching of star formation (e.g. Smethurst et al. 2016; Baron et al. 2017 and references therein). In the case of massive galaxies, the indirect evidence of a past rapid quenching ($<$0.5 Gyr) of the star formation is also provided by the super-solar [α/Fe] and the star formation histories (SFHs) derived for the massive early-type galaxies (e.g. Thomas et al. 2010; McIntosh et al. 2014; Citro et al. 2016; Conroy & van Dokkum 2016).

To summarize, the results obtained so far identified galaxies some time *after* (e.g. post-starbursts) or *before* (e.g. AGN hosts) the quenching of the star formation. However, SF galaxies *during* the quenching phase have not been securely identified. In this paper, we apply a new method aimed at selecting galaxies when their star formation is being quenched. Our search is done at low redshift ($0.04 \leq z < 0.21$) within the SDSS main sample galaxy and is based on the use of higher (i.e. [O III] λ5007, hereafter [O III]) to lower (mainly [O III]/H α) ionization emission line ratios. The modelling and details of the method have been presented by Citro et al. (2017, hereafter C17). In principle, the selection of quenching galaxies is straightforward. After a few Myr from the interruption of star formation, the shortest-lived (i.e. most massive) O stars and their hard UV photons rapidly disappear, and this causes a fast decrease of the luminosity of high ionization lines. However, emission lines with lower ionization should be observable as long as late O and early B stars are still present before they abandon the main sequence (see Fig. 1). Consequently, quenching galaxy candidates can be selected based on the high-to-low ionization emission line ratios. However, the degeneracy between ionization and maximum metallicity makes this approach less straightforward than it looks, and additional criteria should be used to identify the most reliable sample of quenching galaxies. In this paper, we present the definition of the parent sample, the methods applied to mitigate the ionization-metallicity degeneracy, the extraction of the most

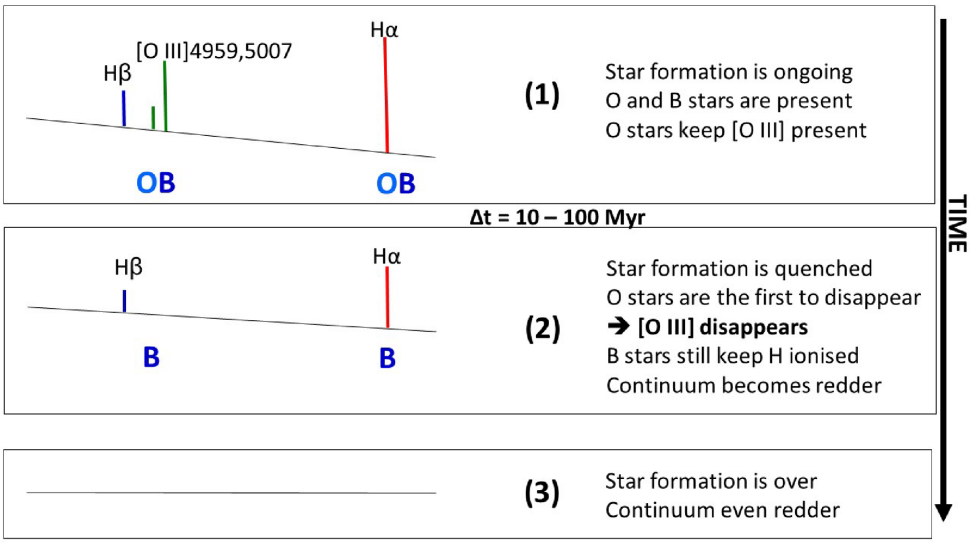

Figure 1. Scheme of the spectral evolution immediately after the quenching. By assuming a sharp quenching model by C17 the delay between phase (1) and (2) is ∼10 Myr and become ∼100 Myr by assuming a smoother and slower star formation decline (with a smoother exponential decline of the star formation with *e*-folding time $\tau = 200$ Myr).

reliable quenching galaxy (QG hereafter) candidates, and the general properties of the selected sample. We assume a flat ΛCDM cosmology with $H_0 = 70\,\mathrm{km s^{-1}\,Mpc^{-1}}$, $\Omega_\mathrm{m} = 0.3$, and $\Omega_\Lambda = 0.7$.

2 THE SAMPLE SELECTION

2.1 The parent sample

Our sample is selected from the Sloan Digital Sky Survey Data Release 8[1] (SDSS-DR8; Aihara et al. 2011), adopting the following criteria:

(i) keyword 'class' = 'GALAXY';
(ii) redshift range $0.04 \leq z < 0.21$;
(iii) keyword 'LEGACY_TARGET1' = 64

The first criterion is clearly used to avoid stars and quasars. The second one is adopted to minimize the biases due to the fixed aperture of SDSS spectroscopy. We identify systems where star formation is being quenched globally across the entire size of the galaxy. In order to ensure that the properties of the galaxy fraction measured inside the fibre aperture are reasonably representative of the global values, Kewley, Jansen & Geller (2005) found that the fibre should cover at least the 20 per cent of the observed B_{26} isophote light of the galaxy. For SDSS, this fraction corresponds roughly to a redshift cut $z > 0.04$. Furthermore, we set an upper limit of $z < 0.21$, beyond which the number of objects rapidly decreases and do not significantly contributes to the sample statistic.

The third criterion ensures a homogeneous selection focusing on the Main Galaxy Sample (see Strauss et al. 2002, for details), therefore avoiding mixing galaxies with different selection criteria.

With the application of these three criteria, our total sample is constituted by 513596 galaxies. This sample is called *parent sample* hereafter, and includes all galaxy types (from passive systems to SF objects) as well as Type 2 AGNs. In order to avoid the spectral contamination due to sky lines residuals, we exclude ∼62400 objects for which the centroids of the main emission lines (i.e. [O II] λ3727 – hereafter [O II], Hβ,[O III], Hα and [N II] λ6584 – hereafter [N II]) are overlapped with the strongest sky lines.

The spectral line measurements and physical parameters of the selected galaxies are obtained from the data base of the Max Planck Institute for Astrophysics and the John Hopkins University (MPA-JHU measurements[2]). In particular, we retrieve the following quantities:

(i) *Emission lines flux*. The fluxes are measured with the technique described in Tremonti et al. (2004), which is based on the subtraction of the (Bruzual & Charlot 2003, BC03) best-fitting population model of the stellar continuum, followed by a simultaneous fit of the nebular emission lines with a Gaussian profile.

(ii) *Uncertainty in emission lines fluxes*. We use the updated uncertainties provided by Juneau et al. (2014), which are obtained comparing statistically the emission line measurements of the duplicate observations of the same galaxies.

(iii) *Stellar mass*. The stellar masses are estimated through SED fitting to the SDSS *ugriz* galaxy photometry, using a Bayesian approach to a BC03 model grid. The magnitudes are corrected for the contribution of the nebular emission lines assuming that these contributions to the broad-band magnitudes *u,g,r,i,z* are the same inside and outside the 3 arcsec fibre of the SDSS spectrograph. The obtained estimates are referred to the region sampled by the fibre. To obtain the total stellar mass, the MPA-JHU group corrected the stellar masses with a factor obtained by the difference between fibre magnitudes and total magnitudes. For this work, we assume the *total stellar masses* corresponding to the median of their Bayesian probability distribution function.

(iv) *Rest-frame absolute magnitude*. The rest-frame absolute magnitudes are derived from the *ugriz* broad-band photometry, and corrected for the AB magnitude system.

(v) *Nebular oxygen abundance*. Nebular oxygen abundance is estimated using a Bayesian approach, adopting the Charlot & Longhetti (2001) models as discussed in Tremonti et al. (2004)

[1]The data were downloaded from the CAS data base, which contains catalogues of SDSS objects (https://skyserver.sdss.org/CasJobs/).

[2]see http://wwwmpa.mpa-garching.mpg.de/SDSS/.

and Brinchmann et al. (2004). The estimates of oxygen abundances are expressed in 12 + log(O/H) values, and were derived only when the signal-to-noise ratio (S/N) in H α, H β, [O III], and [N II] is > 3. In this work, we consider the 12 + log(O/H) value corresponding to the median of the Bayesian probability distribution function.

(vi) *EW(Hα)*. We adopt the rest-frame equivalent widths estimated by the SDSS pipeline with a continuum corrected for emission lines.

(vii) D_n4000 . We use the D_n4000 (Balogh et al. 1999) corrected for emission lines contamination.

(viii) *Galaxy size and light concentration*. The size is represented by the radius enclosing the 50 per cent of the *r*-band Petrosian flux (R50). The light concentration is defined as C=R90/R50, where R90 is the radius containing the 90 per cent of the *r*-band Petrosian flux.

In addition to these quantities, we also collect information about the galaxy *environment* by cross-matching our sample with the catalogue provided by Tempel et al. (2014) that contains environmental information relative to SDSS-DR10[3] and we found a match for about the 87 per cent of galaxies in our sample. In particular, we use the environmental density they provide for each galaxy ($\rho_{\rm env}$, hereafter), which represents an estimate of the overdensity with respect to the mean galaxy density within a scale of 1 h^{-1} Mpc centred on each galaxy. Furthermore, we use their *Richness* and *Brightness Rank*, that are defined, respectively, as the number of members of the group/cluster the galaxy belongs to, and the luminosity rank of the galaxy within the group/cluster.

Finally, we analyse the SDSS morphological probability distribution of the galaxies provided by Huertas-Company et al. (2011),[4] which is built by associating a probability to each galaxy of belonging to one of four morphological classes (Scd, Sab, S0, E).

2.2 The H α emission subsample

As anticipated in Section 1, our aim is to identify galaxies in the critical phase when the star formation is being suppressed. In the case of an instantaneous quenching (see Fig. 1), this translates in searching for SF galaxies where high-ionization lines (e.g. [O III]) are suppressed due to the disappearance of the most massive O stars, whereas Balmer emission lines are still present because their luminosity decrease more slowly due to photo-ionization from lower mass (longer lived) OB stars.

For these reasons, we select a subsample of galaxies with Hα emission considering the following criteria:

(i) EW(H α) and EW(H β) ≤ 0, in order to select galaxies with Balmer emission lines.

(ii) S/N(H α) ≥ 5. For the SDSS this corresponds to objects with H α fluxes above $\simeq 1.1 \times 10^{-16}$ erg s^{-1} cm^{-2}.

(iii) S/N(H β) ≥ 3, to be able to properly correct for dust extinction using the H α/H β ratio. With this criterion, we exclude $\sim$6 per cent of galaxies, and the corresponding limiting flux is $\simeq 3.2 \times 10^{-17}$ erg s^{-1} cm^{-2}.

By construction, the H α sample includes galaxies with S/N(H α) ≥ 5; however, the other emission lines can have a lower S/N. When a line flux has S/N <2, we assign an upper limit to the flux defined as

$$F \leq 2 \times \sigma_F. \quad (1)$$

In the case of [O III], which is the most important signature of quenching in our study, this upper limit corresponds to $F \lesssim 2.2 \times 10^{-17}$ erg s cm^{-2}.

The full H α emission sample contains $^{-1}244362$ objects. Clearly, this sample includes a heterogeneous ensemble of galaxies where emission lines are powered by different ionization processes (SF, type 2 AGNs, LINERs, etc.).

2.3 The subsample of star-forming galaxies

Since we are interested in purely SF systems, we cleaned the H α sample from contaminating galaxies. In order to separate the SF population from objects hosting AGN activity, we use the diagnostic diagram of Baldwin, Phillips & Terlevich (1981, hereafter BPT).

Fig. 2 shows the BPT diagram of our sample. We remind that the emission lines involved in this diagram are close enough in wavelength that the correction for dust extinction is negligible. We adopt the Kauffmann et al. (2003) criterion[5] to reject type 2 AGNs, LINERs, and composite objects from the H α sample. For galaxies, where all lines are detected, the SF population can be easily isolated, while for galaxies where [O III] is undetected (i.e. S/N[O III] <2), we select only those galaxies whose upper limits of [O III] flux lie below the Kauffmann et al. (2003) relation. With this approach, we exclude 62125 AGNs and LINERs, and obtain the final subsample of 174 056 SFgalaxies.

Then, we divide this sample into two subsamples:

SF-Alldet (148145 galaxies). These are SF galaxies where all the main emission lines (H β, [O III], H α, and [N II]) are significantly detected. We, therefore, reject all the objects with S/N([N II]) < 2 (i.e. 241 objects).

SF-[O III] undetected (25 911 galaxies). These galaxies differ from the previous ones for their [O III], that in this case is undetected (i.e. S/N < 2).

unnumlist

In order to compare the SF galaxies with the other galaxy types, we also select a complementary subsample of galaxies without H α emission from the parent sample (Section 2.1). Hereafter, the extracted sample is called **no-H α** subsample, and includes 201527 galaxies with S/N(H α) < 5. Table 1 summarizes the number of galaxies in the different subsamples, while Fig. 3 shows some of the main parameter distributions of the subsamples (i.e. redshift, masses, and colour excess).

2.4 The correction for dust extinction

Since all the SF-Alldet and SF-[O III]undet galaxies have H β with S/N>3, we correct their emission line fluxes for dust attenuation based on the H α/H β ratio, adopting the Calzetti et al. (2000) attenuation law. The colour excess $E(B-V)$ is derived assuming the Case B recombination and a Balmer decrement H α/H β = 2.86 (typical of H II regions with electron temperature $T_e = 10^4$ K and electron density $n_e \sim 10^2$–10^4 cm^{-3}; Osterbrock 1989). For galaxies with H α/H β <2.86 (2072 galaxies, $\sim$1 per cent), i.e. with a negative colour excess, between $\sim -0.2 \leq E(B-V) < 0$, we

[3]The catalogue is available at http://cosmodb.to.ee

[4]We downloaded the SDSS morphological probability distribution of the galaxies together with the Tempel et al. (2014) catalogue.

[5]Their criterion is defined as $\log([\mathrm{O\,III}]/\mathrm{H}\beta) < 0.61/\{\log([\mathrm{N\,II}]/\mathrm{H}\alpha) - 0.05\} + 1.3$.

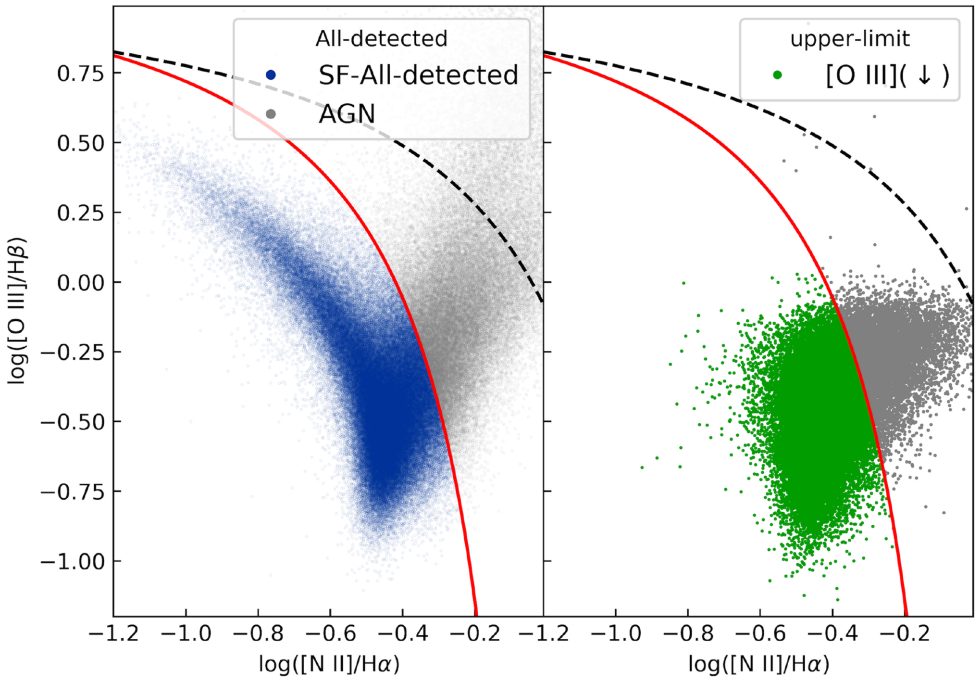

Figure 2. The BPT diagram of the H α subsample. In the left-hand panel we show the diagram for the galaxies whose all the BPT emission lines are detected (i.e. S/N $>$ 5 for H α, S/N $>$ 3 for H β, and S/N $>$ 2 for [O III] and [N II]). The red solid line is taken from Kauffmann et al. (2003), while the black dashed line was determined theoretically by Kewley et al. (2001). The blue dots represent the SF-Alldet galaxies, while the grey ones the AGNs. In the right-hand panel we show the BPT diagram for galaxies with upper limit in [O III] line (i.e. galaxies with S/N([O III]) $<$ 2). The green dots represent those galaxies that, despite their upper limit, satisfy the Kauffmann et al. (2003) criterion for SF galaxies, while the grey ones represent objects for which we cannot be sure about their actual condition.

Table 1. Numbers and median redshift of galaxies in the different subsamples.

Sample	Subsample	Number	Median z
SF-H α		174056	0.08
	SF-Alldet	148145	0.08
	SF-[O III]undet	25911	0.12
no-H α		201527	0.12
Total		375583	0.10

decide to set $E(B-V)=0$. The $E(B-V)$ distribution is shown in Fig. 3.

2.5 The estimate of star formation rate

After correcting the emission lines for dust extinction, we derive the star formation rates (SFRs) for the SF galaxies. The SFR is derived using the H α luminosity and adopting the Kennicutt (1998) conversion factor for Kroupa (2001) initial mass function:

$$\mathrm{SFR} = L(\mathrm{H}\alpha)/10^{41.28}\ [\mathrm{M}_{\odot}\ \mathrm{yr}^{-1}] \quad (2)$$

In order to obtain the total SFRs, we correct the fibre SFRs for aperture effects. Following Gilbank et al. (2010) and Hopkins et al. (2003), we apply an aperture correction A based on the ratio of the u-band Petrosian flux (which is a good approximation to the total flux) to the u-band flux measured within the fibre:

$$A = \frac{f_{\mathrm{tot}}(u)}{f_{\mathrm{fib}}(u)} = 10^{-0.4(u_{\mathrm{fib}}-u_{\mathrm{tot}})} \quad (3)$$

This method provides results which are in good agreement with the measurements of Brinchmann et al. (2004) obtained with a more complex approach (Salim et al. 2007).

3 FINDING THE QUENCHING GALAXIES

3.1 The general approach

In this analysis, we decide to follow the approach discussed in C17 to select galaxies in the phase when the quenching of their star formation takes place. In particular, C17 showed how the ratio of high-ionization (e.g. [O III] and [Ne III] λ3869 – hereafter [Ne III]) to low-ionization (e.g. Balmer lines) lines can be used to identify galaxies as close as possible to the time when the star formation starts to cease. Here, we explore in particular the dust corrected [O III]/H α ratio (see Section 2.4) to select quenching galaxies. This ratio is highly sensitive to the ionization parameter U and hence to the star formation evolutionary phase. In particular, higher values of U correspond to higher ionization and star-formation levels (for a more extensive discussion, see C17). However, $\log([\mathrm{O\,III}]/\mathrm{H}\alpha)$ is also dependent on the metallicity Z of the ionizing stellar population, in the sense that low $\log([\mathrm{O\,III}]/\mathrm{H}\alpha)$ values can be reproduced with both low U or high Z (i.e. ionization-metallicity degeneracy, Z–U hereafter). In order to find QG candidates, it is therefore necessary to mitigate this degeneracy. To address this issue, we devise two independent methods that are described in the following sections.

3.2 Method A

To mitigate the Z–U degeneracy, we first need to find an estimator for the metallicity independent of [O III]. Following C17, we exploit the [N II]/[O II] ratio as metallicity indicator, as suggested e.g. by Nagao, Maiolino & Marconi (2006). Fig. 4 shows the dust corrected [O III]/Hα versus [N II]/[O II] diagram as a function of the metallicity

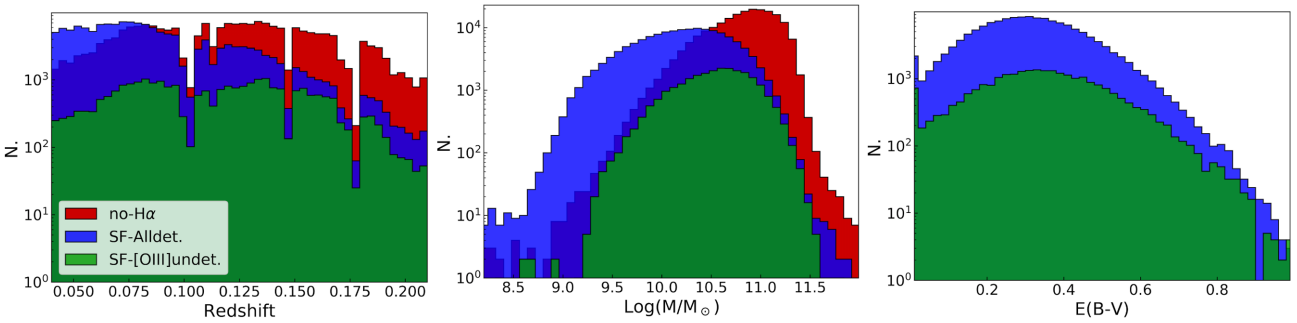

Figure 3. Main distributions of the three main subsamples: SF-Alldet in blue, SF-[O III]undet in green, and no-H α in red: redshift (left-hand panel), masses (central), and colour excess $E(B-V)$ (right).

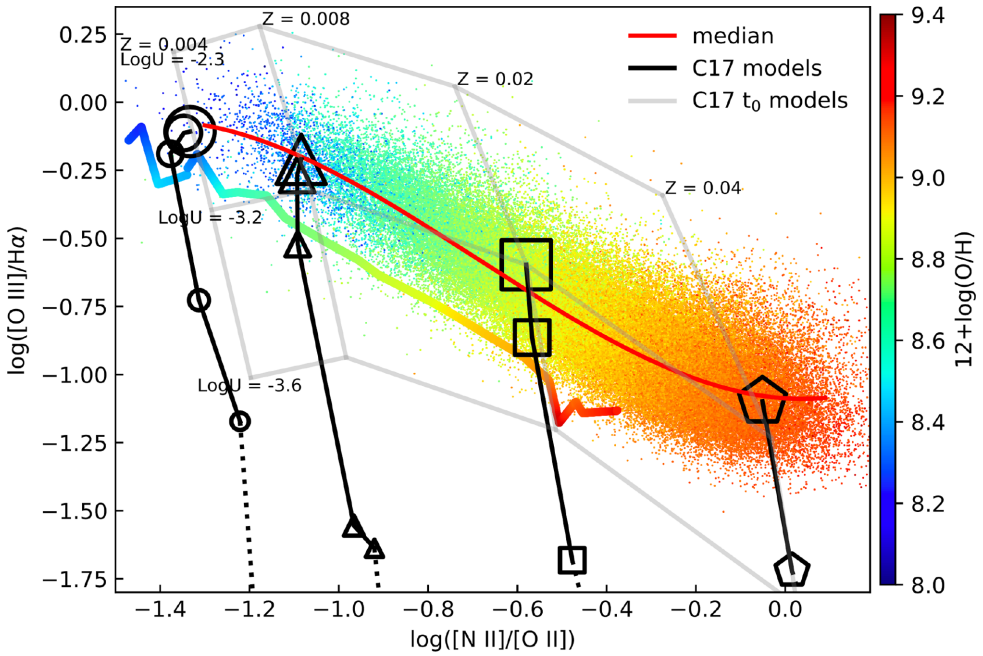

Figure 4. log([O III]/Hα) versus log([N II]/[O II]) diagram. The colour of the dots shows the metallicity estimate 12+log(O/H) by Brinchmann et al. (2004) and the colorful line represents the dispersion at 3σ of the log([N II]/[O II]) for a given value of 12+log(O/H). The red curve represents the median of the relation. Superimposed in grey is reported a grid of zero-ages C17 models with different metallicities and ionization parameters, while in black are shown the evolutive tracks by C17 (circles for $Z = 0.004$, triangle for $Z = 0.008$, square for $Z = Z_{\odot} = 0.02$, pentagon for $Z = 0.04$), where the size of the symbol is reported in time-step of 1 Myr with decreasing sizes.

12+log(O/H). In this analysis,we discard 7712 objects with [O II] undetected (i.e. S/N [O II] < 2).

Fig. 4 clearly shows a very good correlation between [N II]/[O II] and metallicity, with the advantage of having an almost orthogonal dependence between metallicity and log U with respect to the BPT diagram, as confirmed also by the C17 models shown in the figure. This allows to reduce the Z–U degeneracy, since, at fixed [N II]/[O II], the spread of the distribution in [O III]/H α mainly reflects a difference in the ionization status. For comparison, we also show the dispersion at 3σ of the log([N II]/[O II]) at a given 12+log(O/H). In this diagram, therefore, at each [N II]/[O II] (i.e. at fixed metallicity) galaxies with [O III]/Hα lower than the 3σ dispersion due to metallicity can be considered as galaxies approaching the quenching, having an intrinsic lower ionization parameter.

The QG population should represent a population that separates from the SF sequence and starts transiting to the quenched phase. To isolate this extreme population, we analyse the SF-Alldet distribution of [O III]/Hα in slices of [N II]/[O II], searching for an excess of objects (using a Gaussian distribution as reference) with extremely low [O III]/Hα values (i.e. lowest ionization levels; see Fig. 5). A similar approach was used to select starburst galaxies above the main sequence (Rodighiero et al. 2011). We focus in particular on the half part of the Gaussian distribution below the median, not considering the part above since it is dominated by ongoing SF, and could be biased by starburst systems and by a residual contamination of AGNs.

In detail, we proceed as follows:

(i) We divide the distribution in bins of width Δ[N II]/[O II]≈ 0.12 dex.

(ii) In each bin of [N II]/[O II], we estimate the median and the 16th percentile, and describe the distribution of SF-Alldet galaxies with a half-Gaussian whose mean and standard deviation (σ) are fixed to the median and the 16th percentile of the distribution. The typical value of σ is $\sim$0.14 dex.

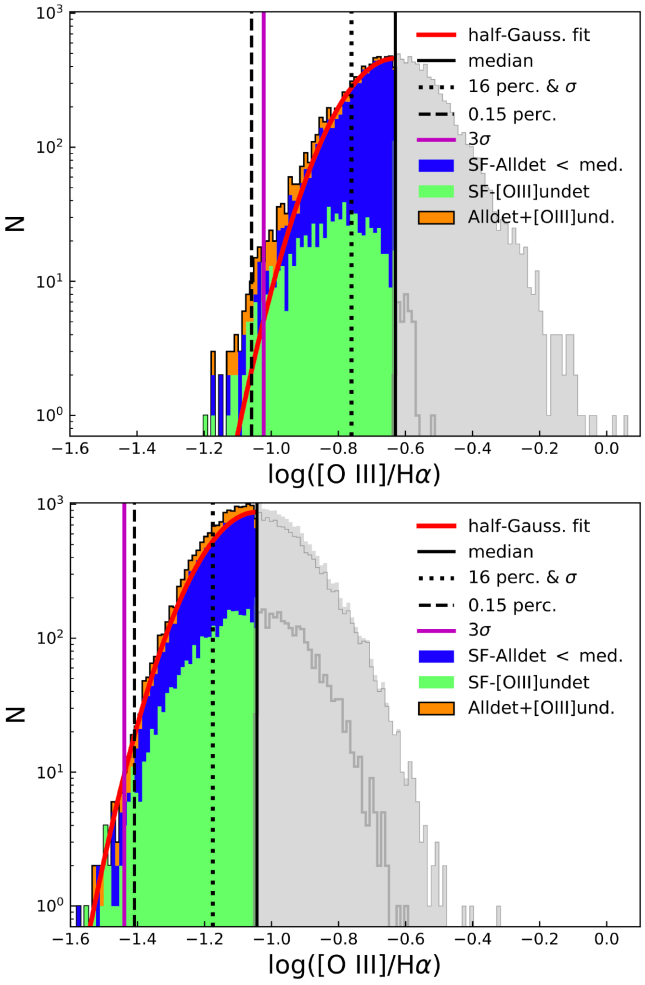

Figure 5. Distribution of [O III]/H α in bins of [N II]/[O II]. For illustrative purposes, we show only two bins, namely $-0.7 \leq \log([\mathrm{N\,II}]/[\mathrm{O\,II}]) < -0.58$ and $-0.2 \leq \log([\mathrm{N\,II}]/[\mathrm{O\,II}]) < -0.08$. The blue and grey histograms represent the distributions of the SF-Alldet galaxies, respectively, below and above the median, and the vertical lines are the median (solid line), the 16th percentile (dotted line), and 0.15th percentile (dashed line) of the distribution. The red solid line shows the Gaussian distribution obtained setting as mean and σ the median and the 16th percentile of the distribution, respectively, and the purple vertical line represents the corresponding 3σ of the half-Gaussian. An excess is identified when the median–3σ of the Gaussian distribution is higher than the 0.15th percentile of the original distribution. The green histogram represents the distribution of the SF-[O III]undet population and in orange we show the contribution of these objects to the global distribution.

(iii) We compare the 3σ value of the Gaussian distribution with the 0.15th percentile, which corresponds to the 3σ value in the case of a Gaussian distribution.

(iv) When the median-3σ value is higher than the 0.15th percentile, i.e. there is a positive detection of a deviation with respect to a Gaussian distribution, we identify our quenching galaxies as the excess beyond 3σ with respect to the half-Gaussian (as shown in the upper panel of Fig. 5).

Following this approach, we find an excess of galaxies in the tail of the distribution in all bins with $\log([\mathrm{N\,II}]/[\mathrm{O\,II}]) < -0.33$ (corresponding to 12+log(O/H) $\lesssim$ 9). Above this threshold, instead, the limiting flux of our sample approaches $\log([\mathrm{O\,III}]/\mathrm{H}\,\alpha) \approx -1.5$, not allowing to detect candidates beyond the 3σ value, as also shown in the bottom panel of Fig. 5.

To provide a less discrete description of the data, we generalize our method deriving the running median, the 16th percentile (representing also the σ of the half-Gaussian), the 0.15th percentile and the median-3σ for our SF-Alldet sample in the [O III]/H α versus [N II]/[O II] plane. We fit these relations with a third-order polynomial,[6] and, to be more conservative, we define our QGs as the SF-[O III]undet galaxies lying below the median-3σ polynomial of SF-Alldet population. This threshold is always below the dispersion in $\log([\mathrm{N\,II}]/[\mathrm{O\,II}])$ at 3σ due to the metallicity (see Fig. 6) and this suggests that the low $\log([\mathrm{O\,III}]/\mathrm{H}\alpha)$ values are not related with the metallicity.

To further clean our sample, we discard also the 10 candidates that have [Ne III] detected, since it is a high-ionization line and its presence is incompatible with the star-formation quenching (see C17).

With this approach, we find 192 QG candidates (hereafter QG-A). Fig. 6 shows the [O III]/H α versus [N II]/[O II] diagram, together with the selected QGs.

A possible issue with this method is that it is based on emission lines that are quite separated in wavelength, and therefore could be affected by inappropriate correction for dust extinction. To test the impact of the extinction law on [O III]/Hα and [N II]/[O II], we consider also the Seaton (1979) extinction law instead of the Calzetti et al. (2000) one, finding a difference in the ratios at most of 0.1 per cent, and therefore not affecting strongly our selection.

We also explore an alternative diagnostic diagram, considering the [O III]/Hβ versus [N II]/[S II],[7] discarding the redshift ranges in which the measurement of [S II] doublet could be biased by strong sky lines. The [N II]/[S II] ratio has metallicity sensitivity similar to the one of [N II]/[O II], and [O III]/Hβ is very similar to [O III]/Hα, with the drawback of H β being weaker than H α. This diagram has the advantage that the pairs of lines involved are close enough that it is possible to neglect the effect of dust extinction. Following the same procedure described above, we select 144 quenching candidates. However, since [S II] is intrinsically weaker than [O II], the S/N([S II]) distribution of these candidates peaks at S/N $\sim$2 and, consequently, their identification is more uncertain. We, therefore, decide not to consider them in the following.

3.3 Method B

An alternative method to mitigate the *Z*–*U* degeneracy is to select galaxies for which [O III] is weaker than the minimum flux expected for the maximum metallicity. In this way, we can safely assume that the observed value of [O III]/Hα is unlikely to be due to high-metallicity. To investigate this possibility, we proceed as follows:

(i) We derive a metallicity estimate (*Z*) for each galaxy in our sample. We exploit the 12+log(O/H) versus [N II]/[O II] relation suggested by Nagao et al. (2006) (see Fig. 7), estimating the running median and the corresponding dispersion σ_Z for the SF-Alldet sample.

[6]Defined $x = \log([\mathrm{N\,II}]/[\mathrm{O\,II}])$ and $y = \log([\mathrm{O\,III}]/\mathrm{H}\alpha)$, the polynomials are: $y(\mathrm{median}) = -1.09 - 0.11x + 1.39x^2 + 0.67x^3$, $y(16\mathrm{perc.}) = -1.22 - 0.09x + 1.48x^2 + 0.76x^3$ and $y(0.15\mathrm{perc}) = -1.47 - 0.21x + 1.04x^2 + 0.53x^3$.

[7][S II] (i.e. [S II]λ6720) represents the sum of [S II]λ6717 and [S II]λ6731 fluxes.

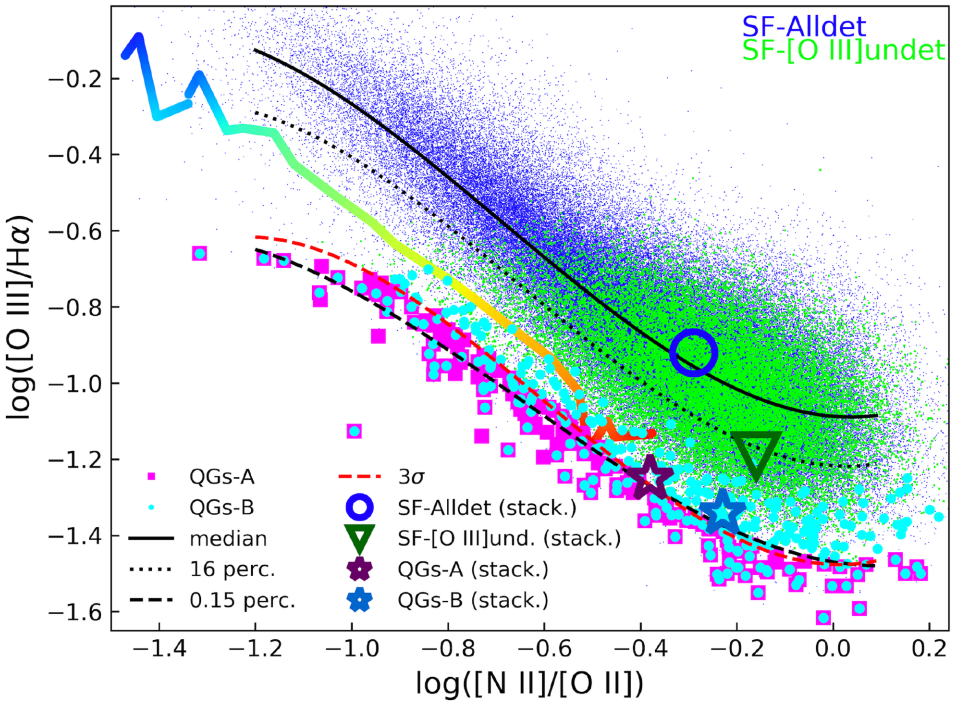

Figure 6. [O III]/H α versus [N II]/[O II] diagram. In blue are shown the SF-Alldet galaxies. The continued black curve represents the median of the relation, while the dotted and dashed ones represent the 16th and 0.15th percentiles, respectively. The dashed red curve represents the dispersion at 3σ of the relation. The superimposed colorful line represents the dispersion at 3σ of the log([N II]/[O II]) for a given value of 12+log(O/H) (as in Fig. 4). In green, instead, are shown the SF-[O III]undet galaxies (i.e. upper limit in [O III]). Bigger dots represent the QG-A (magenta) and the QG-B (cyan). The empty symbols represent the values estimated on the stacked spectra of SF-Alldet (blue circle), SF-[O III]undet (green triangle), QGs-A (purple star), and QGs-B (blue star) samples.

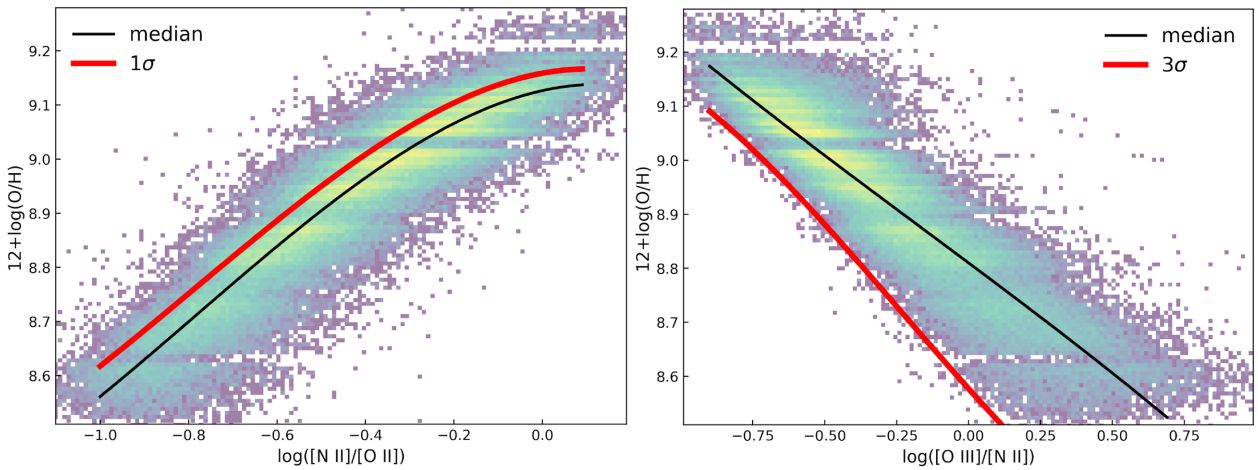

Figure 7. Left-hand panel: 12+log(O/H) versus [N II]/[O II] relation. The black curve represents the median of the relation, while the red curve represents the median $+1\sigma$, where σ is the dispersion of the distribution. Right-hand panel: 12+log(O/H) versus [O III]/[N II] relation. The black curve represents the median of the relation, while the red curve represents the median–3σ.

We therefore associate with each galaxy the median 12+log(O/H) corresponding to the observed [N II]/[O II][8] as metallicity value.

(ii) We estimate the maximum metallicity ($Z_{\rm max}$) of each galaxy, as

$$Z_{\rm max} = Z + \sigma_Z, \quad (4)$$

where Z and σ_Z are the median and the dispersion associated to this relation (with $\sigma_Z \approx 0.13$ dex); since the dispersion would be higher

[8]Note that we evaluate the expected metallicity also for galaxies with [O III] undetected, while Tremonti et al. (2004) derived metallicity only for galaxies with all emission lines detected (i.e. with the original S/N > 3).

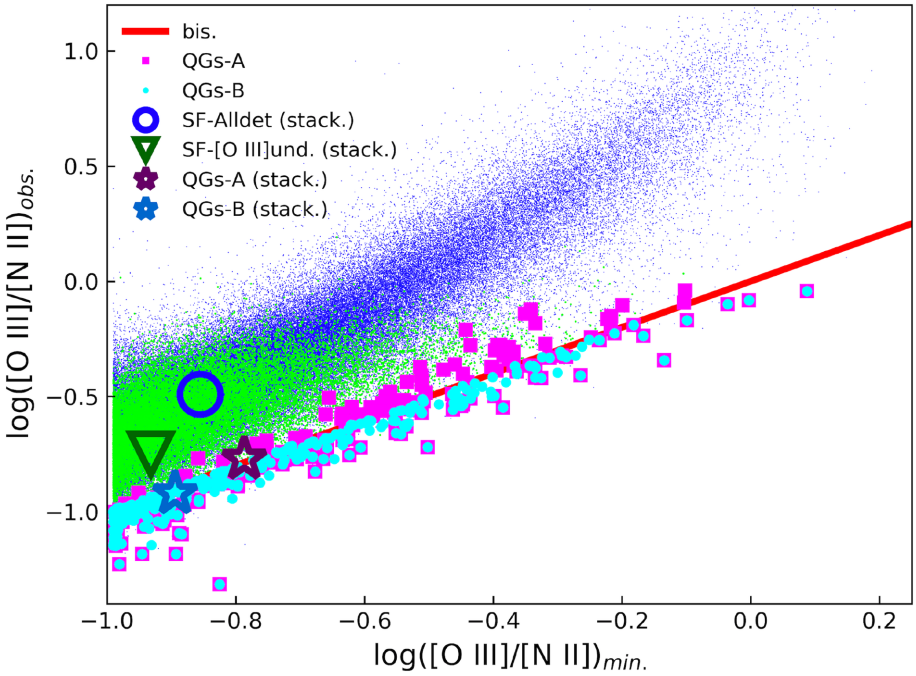

Figure 8. [O III]/[N II]$_{obs}$ versus [O III]/[N II]$_{min}$ diagram. In blue are shown the SF-Alldet galaxies, while in green the SF-[O III]undet galaxies. Bigger dots represent the QG-A (magenta) and the QG-B (cyan). The empty symbols represent the values estimated on the stacked spectra of SF-Alldet (blue circle), SF-[O III]undet (green triangle), QGs-A (purple star), and QGs-B (blue star) samples.

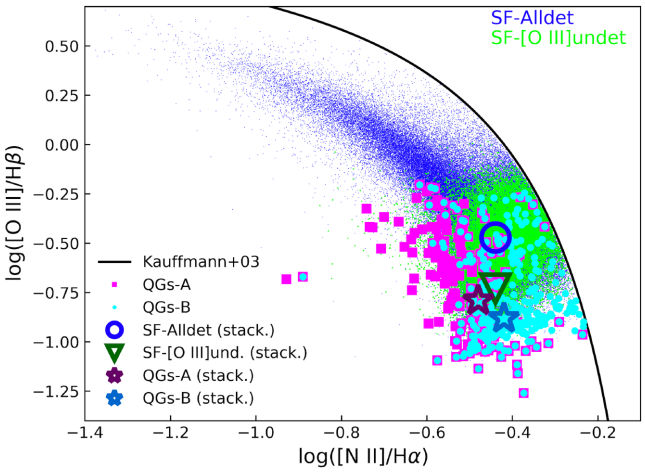

Figure 9. The BPT diagram of our sample galaxies. The colour code is the same of Fig. 8.

than the typical metallicity errors, hence Z_{max} represents a statistical significant estimate for the maximum metallicity.

(iii) In addition, we estimate the minimum expected [O III] flux for any given Z_{max}. To do that, we consider another relation between metallicity and emission lines that includes [O III]. In particular, we adopt [O III]/[N II] as a function of Z (Nagao et al. 2006) (see Fig. 7). This relation allows us to estimate the minimum expected [O III]/[N II] for any given Z_{max}:

$$[\mathrm{O\,III}]/[\mathrm{N\,II}]_{min.} = [\mathrm{O\,III}]/[\mathrm{N\,II}] - 3\sigma_{[\mathrm{O\,III}]/[\mathrm{N\,II}]}, \quad (5)$$

where $\sigma_{[\mathrm{O\,III}]/[\mathrm{N\,II}]}$ is the dispersion of the [O III]/[N II] versus 12+log(O/H) relation (the typical dispersion is $\sigma_{[\mathrm{O\,III}]/[\mathrm{N\,II}]} \approx 0.18$ dex).

(iv) We identify as quenching candidates those galaxies with a [O III]/[N II] lower than [O III]/[N II]$_{min}$. For these galaxies, the low observed values of [O III]/[N II] are unlikely due to their metallicity. Finally, as in method A, we discard 11 galaxies with detected [Ne III], since it can be a sign of ongoing star formation.

In this way, we select 308 'method B' quenching candidates (hereafter QG-B), which are shown in Fig. 8.

3.4 Comparing the two methods

In this section, we explore the differences and the complementarities between the two methods.

We first notice that there are 120 QGs in common between the two methods. In the [O III]/Hα versus [N II]/[O II] diagram (i.e. the plane described in Section 3.2; see Fig. 6) there is a good agreement between Methods B and A: the bulk of QGs-B are located below (∼40 per cent) or close to the 3σ curve that is the threshold criterion to select QGs-A. We also show the location of QGs-A candidates in the diagram used to select QGs-B (Fig. 8). Also in this case there is a good agreement between the two samples, with QGs-A located below (∼60 per cent) or just above the threshold criterion, having slightly higher upper limits for the observed [O III]/[N II]. We could obtain a better agreement just slightly relaxing the thresholds adopted in the two methods. For example, if we adopt 2.5σ as thresholds instead of 3 for both methods, we obtain that about 60 per cent and 70 per cent of QGs-B are identified also as QGs-A and vice versa. More conservative choices guarantee, however, to obtain more solid results and higher purity at the cost of a lower overlap. Moreover, the residual discrepancy is due to an intrinsic difference between the two methods that leads to select quenching candidates with different but complementary characteristics. In Fig. 9 we show the BPT diagram with the candidates selected from the two methods. The bulk of QGs-A are distributed in the

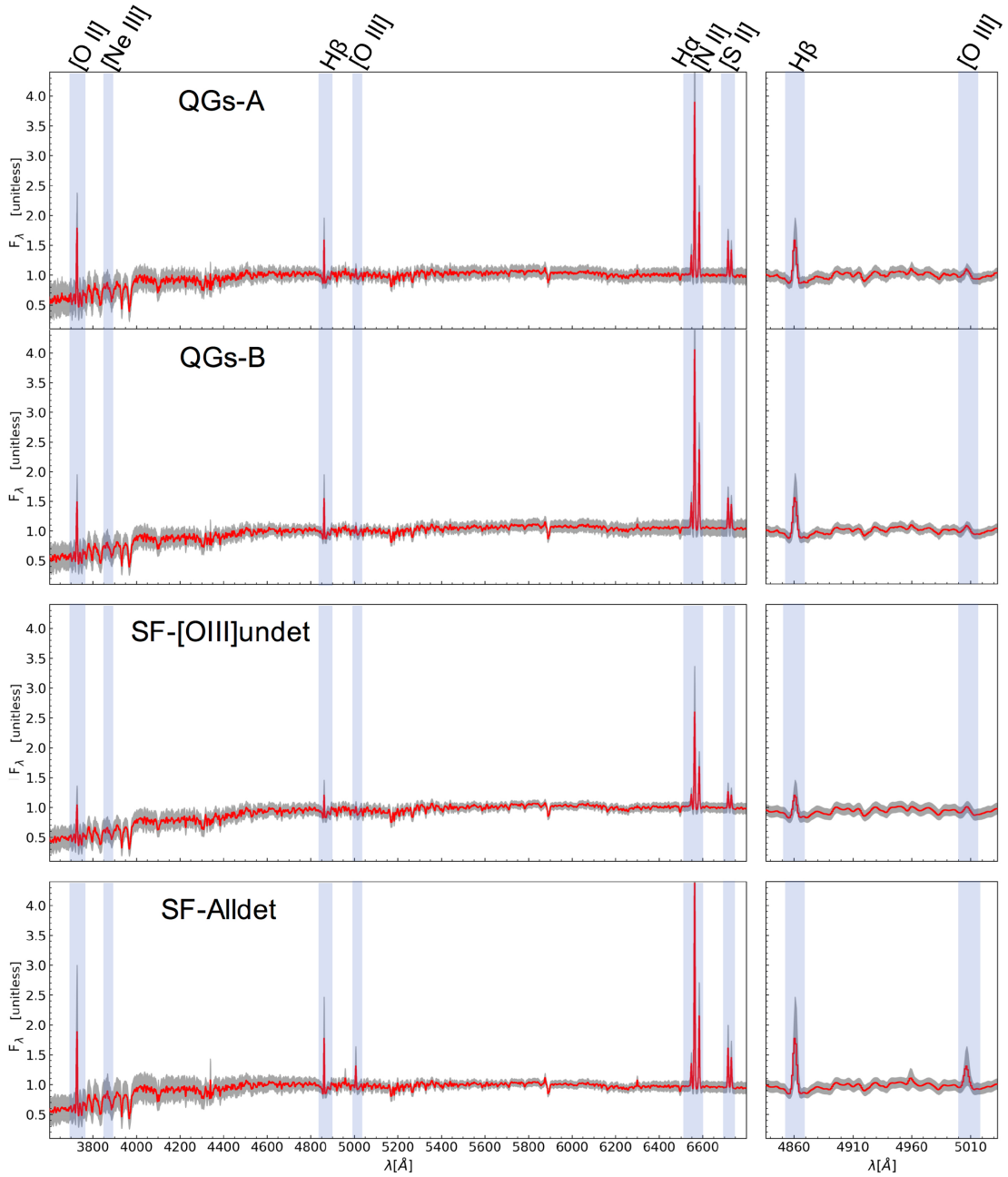

Figure 10. The median stacked spectra (in red) of QGs-A, QGs-B, SF-[O III]undet, and SF-Alldet galaxies. The grey shaded area represents the dispersion of the stacked spectra. The percentiles of the redshift distributions of galaxies in each stacked spectrum are listed in Table 3.

lower envelope of the BPT diagram at log([O III]/H β)$<$ 0 and log([N II]/H α)$<$ -0.3, while QGs-B are complementary located in a region at higher [N II]/H α values (log([N II]/H α)$>$ -0.5).

4 THE PROPERTIES OF QUENCHING GALAXIES

In this section we analyse the properties of the QGs in order to identify or to constrain plausible quenching mechanism.

In Table 3 we report the median, the 16th and 84th percentiles of the distribution of the main properties of our QGs, compared with those of the three control samples defined in Section 2.3: SF-Alldet, SF-[O III]undet, and no-Hα. We first notice that the median and the range in redshift of QGs candidates are similar to that of SF galaxies (SF-Alldet). On the contrary, SF-[O III]undet and no-Hα sample cover different redshifts ranges.

4.1 Spectral properties

We first inspect the spectra of our QG candidates. In order to increase their S/N, in particular around [O III] and [Ne III] to confirm their low ionization status, we stack their spectra. Fig. 10 shows the median-stacked spectrum of QGs-A and QGs-B. As a comparison, we show also the spectra of two control samples, stacking all galaxies from SF-Alldet and SF-[O III]undet samples, respectively, in the same mass and redshift range of QGs. The [O II], H α, and H β lines (i.e. low-ionization lines) are the strongest emission lines, while [O III] and [Ne III], which are high-ionization emission lines, are very weak

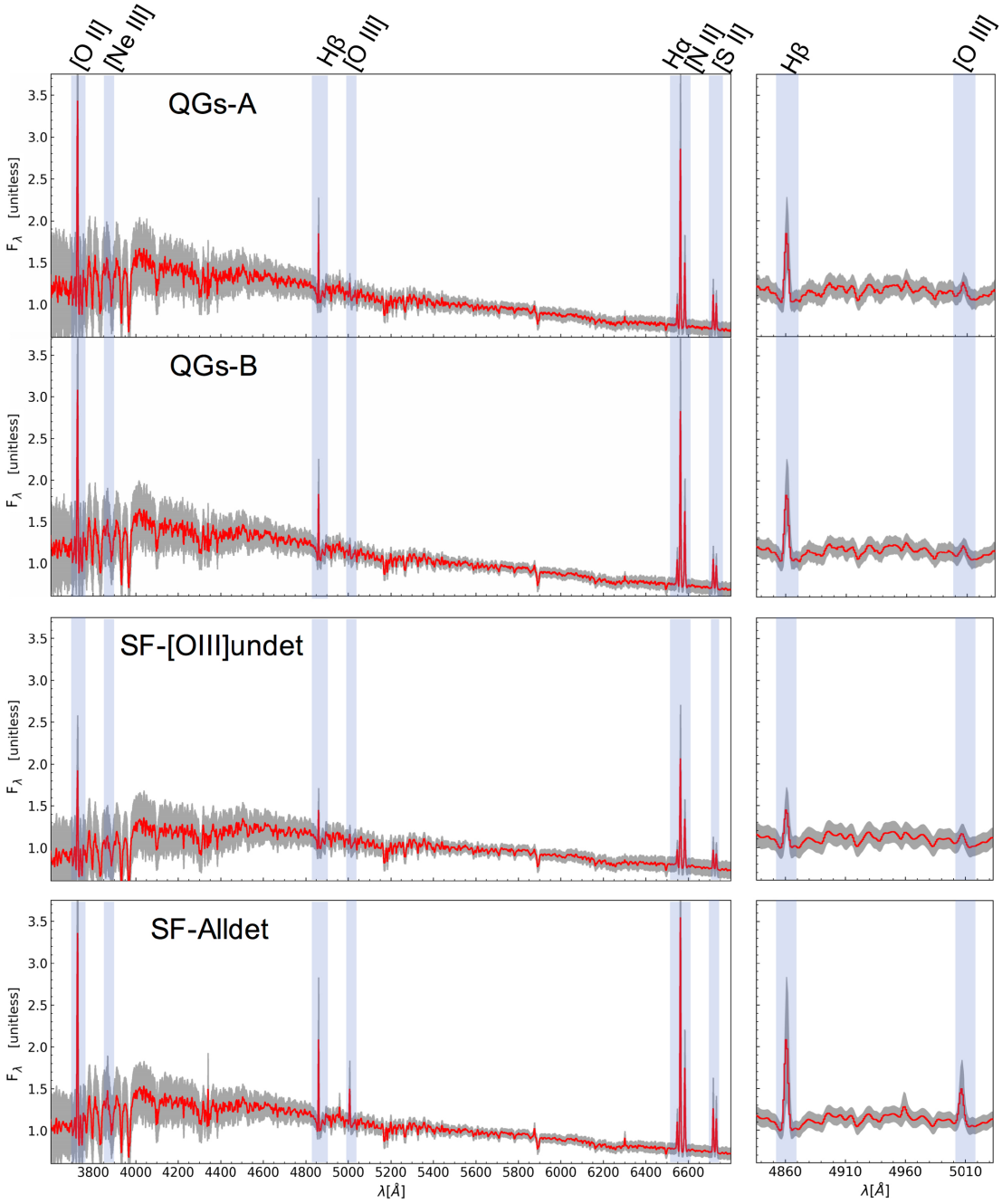

Figure 11. The median-stacked spectra corrected for the dust extinction (in red) of QGs-A, QGs-B, SF-[O III]undet, and SF-Alldet galaxies. The grey-shaded area represents the dispersion of the stacked spectra. The percentiles of the redshift distributions of galaxies in each stacked spectrum are listed in Table 3.

in both QGs stacked spectra despite the increased S/N (see the zoom of the stacked spectra in the wavelength range around the [O III] and the H β lines).

Furthermore, in order to measure high-to-low ionization emission line ratio and confirm the low ionization level of our QGs, we derive the dust-corrected stacked spectrum, correcting the individual spectra for the dust extinction[9] before stacking them together (see Fig. 11). Also in this case we confirm the weakness of [O III] (and of other high-ionization emission lines, such as [Ne III]) in both QGs stacked spectra. We, further, note that in QGs spectra the stellar continuum is blue, suggesting a still young mean stellar population, consistent with a recent quenching of the star formation (see C17 for discussion on the expected colours of QGs).

We run the *Gandalf* code (Cappellari & Emsellem 2004; Sarzi et al. 2006) on the dust-corrected stacked spectra. We fit the continuum with the stellar population synthesis models of Bruzual & Charlot (2003), used also by Tremonti et al. (2004), and measure the main emission lines and spectral properties on the stacked spectra. We list them in Table 2 and show them in Figs 6, 8, 9, and 12.

[9]We derive it from the H α/H β flux ratio using the Calzetti et al. (2000) extinction law, the same that we have adopted for the dust correction of the emission lines.

Table 2. Main emission lines ratios measured on stacked spectra of QGs-A, QGs-B, SF-[O III]undet, and SF-Alldet samples.

Property	QGs-A	QGs-B	[O III]und.	SF-Alldet
log([O III]/H α)	-1.25 ± 0.04	-1.34 ± 0.04	-1.19 ± 0.02	-0.92 ± 0.04
log([N II]/[O II])	-0.23 ± 0.02	-0.29 ± 0.02	-0.16 ± 0.02	-0.29 ± 0.02
log([O III]/H β)	-0.79 ± 0.04	-0.88 ± 0.04	-0.73 ± 0.03	-0.47 ± 0.02
log([N II]/H α)	-0.48 ± 0.02	-0.42 ± 0.02	-0.44 ± 0.02	-0.44 ± 0.04
log([O III]/[N II])	-0.77 ± 0.03	-0.92 ± 0.03	-0.75 ± 0.02	-0.49 ± 0.02
D_n4000	1.23 ± 0.01	1.25 ± 0.01	1.34 ± 0.01	1.23 ± 0.01
EW$_{rf}$(Hα) [Å]	-18.62 ± 0.09	-18.19 ± 0.07	-12.30 ± 0.01	-21.38 ± 0.01

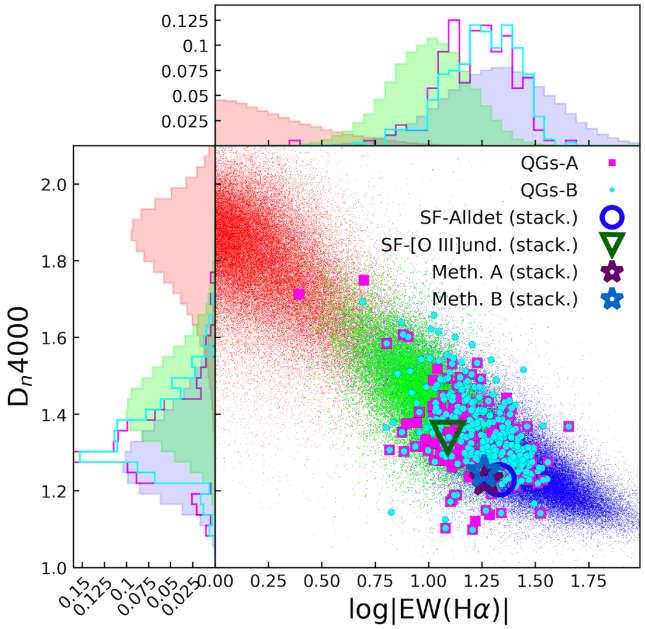

Figure 12. The D_n4000 as a function of the EW(Hα). The layout is the same of Fig. 8.

From this analysis, we find evident H α emission in QGs stacked spectra, although slightly weaker than in the SF, and given that the samples have similar median redshift, we find that $\frac{L(H\alpha)_{QGs\text{-}A}}{L(H\alpha)_{SF\text{-}Alldet}} = 0.82 \pm 0.07$, while $\frac{L(H\alpha)_{QGs\text{-}B}}{L(H\alpha)_{SF\text{-}Alldet}} = 0.91 \pm 0.08$. Further, we measure, in particular, the [O III]/H α and [N II]/[O II] ratios of the median stacked spectra (see Table 2), obtaining values consistent with the low ionization level of our QG candidates and far below the control sample of SF galaxies. We note, instead, that the [O III]/H α value measured on the SF-[O III]undet stacked spectrum is intermediate between SF and QG candidates, suggesting that also SF-[O III]undet galaxies have a lower ionization state with respect to the SF population, but not as extreme as QG candidates. In Figs 6, 8, and 9 we show the ratios measured on stacked spectra. In particular, from Figs 6 and 8 we confirm that the ratios measured on stacked spectra of QGs are consistent with both our selection criteria and a low-ionization state, while the ratios for SF galaxies lie consistently on their median relations, compatible with ongoing star formation (see Fig. 4 and C17). Finally, we note that the ratios for SF-[O III]undet lie only slightly above our selection criteria, suggesting a lower ionization level with respect to SF galaxies. This also indicates that also amongst these galaxies there are good QG candidates. In this case, the limiting flux of the survey does not allow to pre-select individual QG candidates from single spectra, and to separate them from a residual contamination of SF galaxies. From this analysis, we also confirm that QGs-A have slightly higher [O III]/H α and [O III]/[N II] values, and slightly lower [N II]/[O II] and [N II]/H α values compared to QGs-B, suggesting a lower value for their metallicity, consistently with, on average, lower masses (see Section 4.2). We further note that the [N II]/[O II] ratios of our QGs are in both cases similar to those of the SF-Alldet sample, suggesting that our QGs have metallicities similar to the ones of the SF galaxies parent sample.

4.1.1 D$_n$*4000 versus EW(H* α*)*

In this subsection we analyse two spectral features of QGs. The rest-frame equivalent width EW(H α) that represents an excellent indicator of the presence of young stellar populations (e.g. Levesque & Leitherer 2013) and of the specific SFR (sSFR), and the break at 4000 Å rest-frame, that provides an estimate of the age and metallicity of underlying stellar populations (e.g. Moresco et al. 2012). Using them jointly allows to qualitatively evaluate the connection between the newborn stars and the mean stellar population of the galaxy.

In Fig. 12 we show the relation between the D_n4000 and log(|EW(H α)|). Some interesting trends emerge from it. As expected, there is a strong anticorrelation between these quantities and a clear separation of the no-H α galaxies from the SF ones. Furthermore, we note that the SF-[O III]undet sample is shifted towards higher D_n4000 and lower log|EW(H α)| with respect to the distributions of the SF-Alldet sample. This suggests that the SF-[O III]undet galaxies are characterized, on average, by older stellar populations than the SF-Alldet ones. Finally, we find that both QGs-A and -B lie in a region between the bulk of SF-Alldet and the SF-[O III]undet. Interestingly, a few QGs show an intermediate EW(H α) but very low D_n4000 that could be a fingerprint of recent star-formation quenching. We confirm these differences by the measurements from the stacked spectra, i.e. the values of D_n4000 and log(|EW(H α)|) of QGs-A and -B are intermediate between SF-Alldet and no-H α sample (see values reported in Table 3 and Fig. 12).

The different distribution of these populations in both D_n4000 and EW(H α) is also confirmed by Kolmogorov–Smirnov tests (hereafter KS) at high significance level.

This analysis suggests that our QG candidates have stellar populations which are intermediate between SF and already quenched galaxies, confirming that they are interrupting their SF.

4.2 QGs in the colour-mass diagram

Fig. 13(a) shows the rest-frame, dust-uncorrected colour (u–r) as a function of stellar mass. Our SF-alldet sample forms the well-known blue cloud, while the complementary sample of no-H α emission sample shapes the red sequence. The SF-[O III]undet sample overlaps with the blue cloud in the intermediate region between the two

Table 3. Fundamental properties of the QGs, compared against three control samples: SF-Alldet, SF- [O III]undet (the subsample in which the candidates are selected), and no-H α. For each parameter we report the 50th (16th, 84th) percentiles of its distribution.

Property	QGs-A	QGs-B	SF-[O III]undet	SF-Alldet	no-H α
N	192	308	25911	148145	201527
Redshift	0.08 (0.05, 0.11)	0.08 (0.06, 0.13)	0.12 (0.07, 0.16)	0.08 (0.05, 0.13)	0.12 (0.08, 0.16)
$\log(M/M_{\odot})$	10.1(9.7, 10.6)	10.4 (10.1, 10.8)	10.6 (10.1, 10.9)	10.2(9.7, 10.7)	10.9 (10.4, 11.2)
$(u–r)_{rf}$ obs.	1.73(1.53, 2.10)	1.88(1.61, 2.40)	1.93(1.69, 2.27)	1.68(1.38, 2.05)	2.57(2.37, 2.75)
$E(B-V)$	0.40(0.26, 0.59)	0.45(0.30, 0.68)	0.34(0.19, 0.51)	0.31(0.17, 0.46)	/
SFR [$M_{\odot}$ yr^{-1}]	0.33(0.08, 1.63)	0.78(0.22, 2.88)	0.38(0.09, 1.31)	0.47(0.12, 1.75)	0.03(0.01, 0.08)
log(sSFR) [yr^{-1}]	−10.6 (−11.0, −10.3)	−10.5 (−10.8, −10.2)	−11.0 (−11.4, −10.6)	−10.5 (−10.9, −10.1)	−12.4 (−12.7, −11.9)
C(R90/R50)	2.20(2.01, 2.53)	2.28(2.05, 2.62)	2.19(1.97, 2.55)	2.27(2.04, 2.60)	2.86(2.52, 3.13)
D_n4000	1.31(1.25, 1.41)	1.34(1.27, 1.45)	1.43(1.33, 1.55)	1.30(1.20, 1.42)	1.84(1.70, 1.95)
EW$_{rf}$(Hα) [Å]	−16.9 (−24.4, −11.6)	−18.1 (−26.1, −12.0)	−10.1 (−15.3, −6.5)	−21.2 (−37.8, −11.8)	−0.8 (−2.1, −0.2)

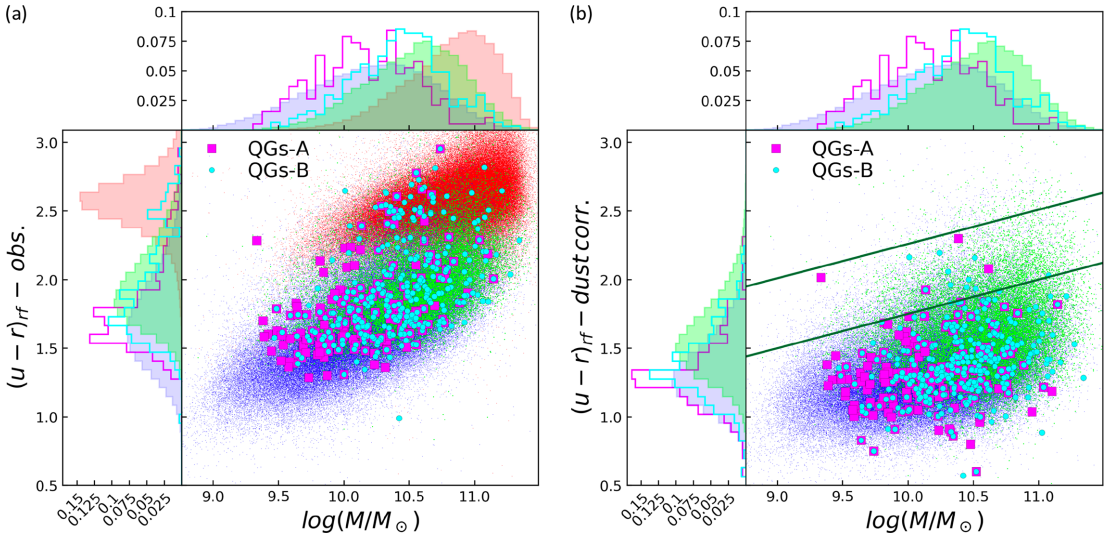

Figure 13. (a) The rest-frame (u–r) colour – mass diagram. The colours are not corrected for the dust extinction. (b) The same diagram with colours corrected for the dust extinction. We represent the SF-alldet subsample with small blue dots, the SF-[O III]undet subsample with small green dots and the control sample of galaxies with no-H α emission with small red dots. We use magenta squares for QGs-A and cyan circles for QGs-B. The two dark green straight lines represent the edge of the green valley defined by Schawinski et al. (2014).

sequences. The QGs-A are mainly located in the blue cloud region at colours $1.5 \lesssim$ (u–r) $\lesssim 2.1$, while only a few of them have redder colours, near or in the lower part of the red sequence. We verify that the red colours of these QGs are due to a strong dust extinction (see following discussion and Fig. 14). The colours of QGs-B have instead a larger spread ($1.6 \lesssim$ (u–r) $\lesssim 2.4$), with a median value redder than the SF-Alldet sample and QGs-A, but still blue. Their colour distribution presents also a significant tail reaching the red sequence [15.9 per cent of the sample has colours (u–r) >2.4]. As for QGs-A, we verify that these red candidates are reddened by dust extinction (see Fig. 14).

In Fig. 14 we show the observed (u–r) colour as a function of the $E(B-V)$ derived from the H α/H β ratio, in order to analyse the contribution of the dust extinction to the colour distribution. Obviously, the no-H α control sample is not included, since its galaxies have S/N(H α) and S/N(H β) lower than 3. There is a clear correlation between colour and $E(B-V)$, also in QGs samples, with the reddest galaxies having the highest values of $E(B-V)$. About 16 per cent of QGs-A show $E(B-V)$ higher than 0.6, while the same percentage of QGs-B have even higher dust extinction, showing $E(B-V) > 0.7$. As anticipated, the QGs with the reddest colours are those with the highest $E(B-V)$ values, which confirm that their intrinsic colours are still blue, as expected from their recent quenching phase (see also the discussion in C17).

In order to better distinguish the dust-reddened quenching candidates from the intrinsic red ones, we exploit the Holden et al. (2012) rest-frame dust-uncorrected colour–colour plane (u–r) versus (r–z), showing the results in Fig. 15. Only a few candidates are located in the region of pure passive red galaxies, whose boundaries are defined by Holden et al. (2012). On the contrary, the other red candidates are actually reddened by the dust extinction.

Finally, Fig. 13(b) shows the colour-mass diagram with the (u–r) corrected for the dust extinction. In particular, we adopt the attenuation law of Calzetti et al. (2000), with the stellar continuum colour excess $E_S(B-V) = 0.44\,E(B-V)$. As already shown, we confirm that none of our QG candidates has intrinsic red colours and only a few of them lie in the green valley region defined by Schawinski et al. (2014). However, although they are mainly in the blue cloud, their colour distributions are different from that of SF-Alldet, showing a peak at $(u-r) \sim 1.3$ and on average redder colours (see Fig. 13b). This is also confirmed by the KS test at a significance level $\alpha = 0.05$.

We stress here that most of our QG candidates would not be selected using dust-corrected green colours, i.e. they do not lie

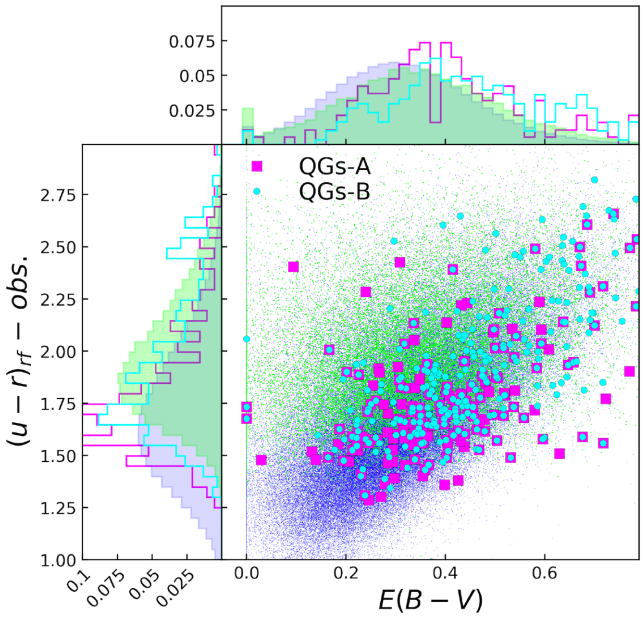

Figure 14. The (u–r) colours as a function of the $E(B-V)$. The layout is the same of Fig. 13.

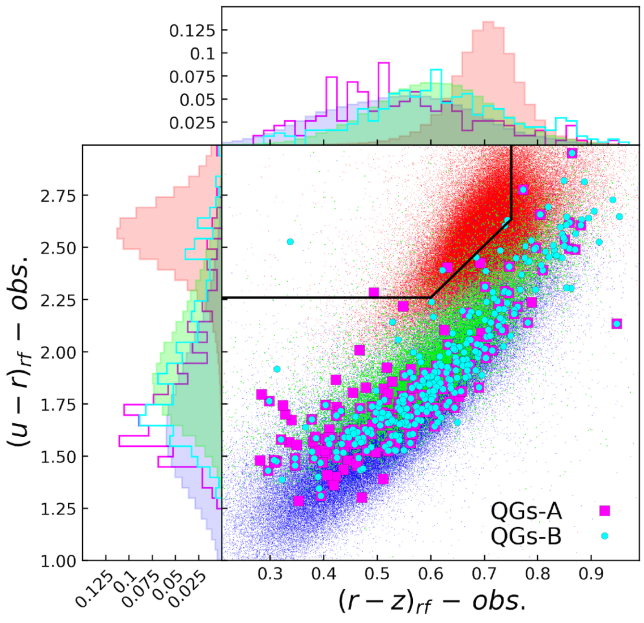

Figure 15. The rest-frame dust-uncorrected colours (u–r) – (r–z) diagram. The layout is the same of Fig. 13. The boundary in black is from Holden et al. (2012).

within the so-called 'Green Valley', which separates SF galaxies from quiescent passive ones.

From our analysis we find that the mass distribution of QGs-A is spread (i.e. 16th–84thpercentiles) over the range $9.8 \lesssim \log(M/M_{\odot}) \lesssim 10.6$, being comparable with that of SF-Alldet galaxies ($9.7 \lesssim \log(M/M_{\odot}) \lesssim 10.7$), however, QGs-A are slightly less massive than the global SF-[O III]undet sample ($10.1 \lesssim \log(M/M_{\odot}) \lesssim 10.9$). The masses of QGs-B are in the range $\sim 10 < \log(M/M_{\odot}) < \sim 10.8$, i.e. they are more massive than those derived by method A. These evidences are also confirmed by the KS test at a significance level $\alpha = 0.05$, verifying that the masses of QGs-A and SF-Alldet are

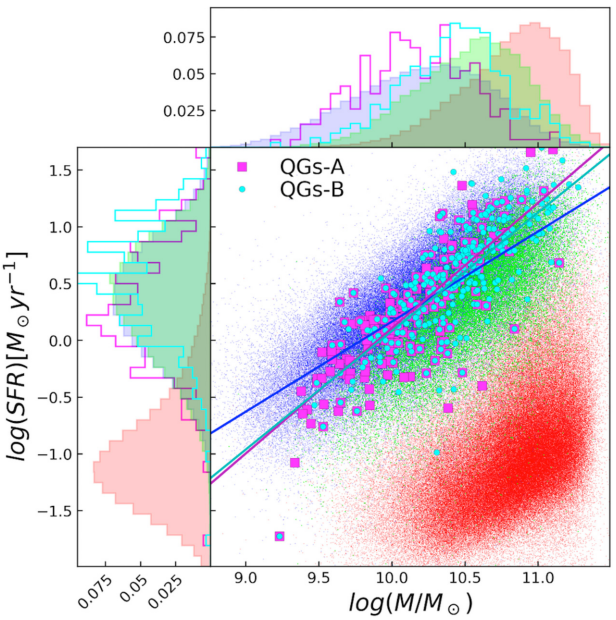

Figure 16. The $\log(SFR_{tot})$ as a function of the stellar mass. The layout is the same of Fig. 13.The blue straight line represents the main sequence (MS) of the SF-Alldet sample, while the magenta and cyan ones are the MS of QGs-A and QGs-B, respectively.

drawn from the same distribution (i.e. p-value = 0.052), differently from that of QGs-B. Moreover, both the QGs masses have distributions which are different from that of [O III]undet. Furthermore, we note that no QG candidates have masses lower than $\log(M/M_{\odot}) < \sim 9.5$ for both methods (A and B). This suggests that, as expected in a downsizing scenario, quenching has not started yet for the low-mass galaxies. This is supported also by the lack of a population of low-mass red galaxies among our no-Hα sample in the red sequence.

4.3 Star formation rates

Fig. 16 shows the SFR-mass plane of our samples. As described in Section 2.1, the SFR is estimated from the dust-corrected H α luminosity. For the no-H α sample, instead, the SFRs are derived from a multiband photometric fitting. We stress, however, that for the QG candidates these SFR estimates should be considered as upper limits to their current SFR, due to their past SFR preceding the quenching. Indeed, even when the O stars die, the longer-lived B stars have sufficient photons harder than 912 Å to ionize hydrogen, explaining their H α emission. In this case their H α emission can be considered as an upper limit to their current SFR. As expected, our SF-Alldet sample forms the well-known SF main sequence[10] (MS), while the SF-[O III]undet sample lies just below it, but it is well separated and above the no-H α sample of low-SFR/passive galaxies. We find that both QGs-A and -B show high SFRs, with only few of them having very low SFRs, compatible with them being already passive. The QGs-A sample has SFR in the range $0.6 < \mathrm{SFR}\ [M_{\odot}\ \mathrm{yr}^{-1}] < 11.5$, with a distribution similar to that of

[10]The straight line representing the SF-Alldet MS is $\log(\mathrm{SFR}) = 0.79 \times \log(M/M_{\odot}) - 7.74$.

Table 4. The 50th (16th, 84th) percentiles of the morphological probability distribution of QGs-A and QGs-B, compared against three control samples: SF-Alldet, SF-[O III]undet (the subsample in which the QGs are selected) and no-H α.

	P(Scd)	P(Sab)	P(S0)	P(E)
QGs-A	0.35 (0.13,0.70)	0.30 (0.17,0.60)	0.04 (0.01,0.14)	0.01 (0.00,0.03)
QGs-B.	0.25 (0.12,0.65)	0.35 (0.18,0.65)	0.05 (0.02,0.22)	0.01 (0.01,0.04)
SF-Alldet	0.33 (0.14,0.65)	0.35 (0.19,0.61)	0.06 (0.03,0.20)	0.01 (0.01,0.04)
SF-[O III]undet	0.27 (0.07,0.66)	0.34 (0.15,0.67)	0.04 (0.01,0.14)	0.01 (0.00,0.03)
no-Hα	0.06 (0.03,0.23)	0.13 (0.04,0.58)	0.19 (0.09,0.61)	0.05 (0.01,0.72)

the SF-Alldet galaxies[11] (see Table 3), but above the SF-[O III]undet galaxies. These pieces of evidence are confirmed by KS tests with a significance level $\alpha = 0.05$. Instead, the KS tests show that the SFR distribution of QGs-B and SF-Alldet are different. This result arises also from the 16th–84thpercentilesof the distribution (see Table 3), where the SFRs of QGs-B are slightly shifted towards higher SFR than those of the SF-Alldet population. This effect is mainly due to the higher average mass for QGs-B sample.

From this analysis we also stress that most of our QG candidates would not be selected as intermediate between SF and passive quiescent ones from the SFR-mass plane.

4.4 Morphology

In this section we analyse the morphologies of our quenching candidates. The favourite scenario for the transformation of SF galaxies into passive ones suggests both the migration from the blue cloud to the red sequence and the morphological transformation from discs to spheroids (e.g. Faber et al. 2007; Tacchella et al. 2015). It is still unclear if this transformation occurs during the migration or via dry merging, when a galaxy has already reached the red sequence. Our QGs samples, catching the galaxies in an early phase after SF quenching, are therefore crucial to address this open question.

In Table 4 we report the 16th–50th–84thpercentiles of the morphological probability distribution of the four morphological classes (Scd, Sab, S0, E) for our subsamples. In Fig. 17 we further show the distribution built assigning to each galaxy the morphological class with the highest probability. SF-Alldet and SF-[O III]undet galaxies have the same distribution: roughly 50 per cent of SF objects are late Scd galaxies, while 40 per cent of them are Sab and less than 10 per cent are S0. On the contrary, the no-H α sample shows a different distribution, in which the early-type classes are more common than the late-type ones. For comparison, the bulk of QGs-A are Scd (∼60 per cent), while 35 per cent are Sab. Also QGs-B are disc galaxies with a similar probability of being disc-dominated Scd galaxies or bulge-dominated Sab disc galaxies. Only ∼7 per cent of QGs-A and ∼10 per cent of QGs-B are instead S0 or E galaxies. Therefore, we conclude that our candidates have the same morphology classes as the SF galaxies. Therefore, our analysis suggests that

[11]The straight lines representing the QGs MS are $\log(SFR) = 1.10 \times \log(M/M_{\odot}) - 10.93$ and $\log(SFR) = 1.04 \times \log(M/M_{\odot}) - 10.36$, respectively, for QGs-A and -B.

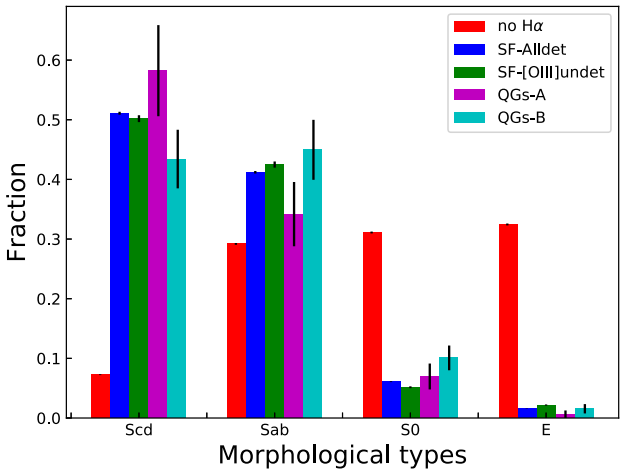

Figure 17. Distribution of no-H α (red), SF-Alldet (blue), SF-[O III]undet (green), QGs-A (magenta), and QGs-B (cyan) in fourmorphological types (Scd, Sab, S0, and E).

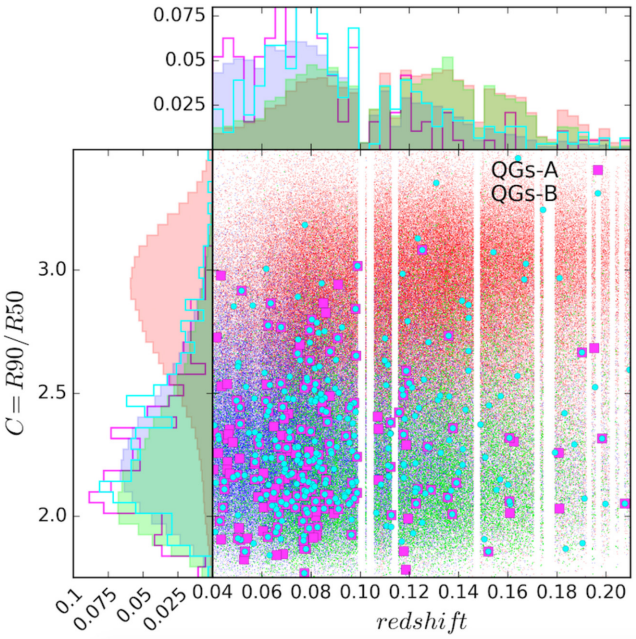

Figure 18. The light concentration–redshift relation for our sample and QGs. The layout is the same of Fig. 13.

no morphological transformation has yet occurred in the early phase after the quenching of the SF.

We further analyse the concentration-redshift relation, shown in Fig. 18. The concentration is defined as C=R90/R50, where R90 and R50 are the radii containing 90 and 50 per cent of the Petrosian flux in *r* band. This parameter is strongly linked to the morphology of the galaxies, and there is general consensus that $C = 2.6$ is the threshold concentration dividing early-type galaxies from the other types (e.g. Strateva et al. 2001). This value is, indeed, confirmed by the crossing point between the C distributions of our SF and no-Hα samples. The bulk of QGs have C <2.6, but some of them (∼12 per cent of QGs-A and ∼17 per cent of QGs-B) have higher concentrations. This suggests that they could be quenching galaxies which have experienced morphological transformation during the transition from blue cloud to red sequence.

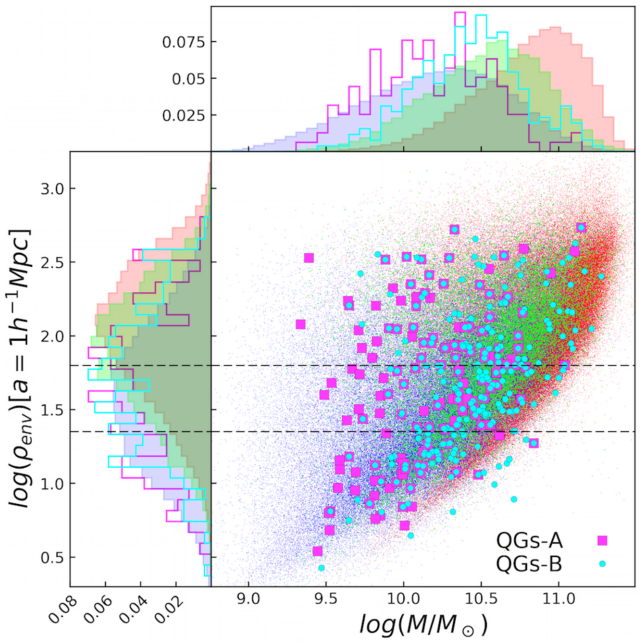

Figure 19. Normalized environmental density of galaxies $\rho_{\rm env}$ (smoothing scales of $1\,h^{-1}$ Mpc) versus stellar mass. The two dashed lines (at $\rho_{\rm env} = 22.45$ and $\rho_{\rm env} = 62.87$, respectively) divide the SF-Alldet $\rho_{\rm env}$ distribution into three tertiles.

4.5 Environment

In this section, we examine the environment of our sample of QGs. Studying the local environment of a galaxy is crucial to disentangle between several known mechanisms able to remove the cool gas needed for star formation.

Fig. 19 shows the 'environmental density' of galaxies $\rho_{\rm env}$ normalized at a smoothing radius of $1\,h^{-1}$ Mpc (see Section 2.1), as a function of stellar mass. It is possible to note a general trend, but with a wide spread, in which the highest stellar mass of the galaxies increases for increasing density and this behaviour is true also for our QGs. We note, in particular, that at the highest densities there are QGs with a large mass spread, while low-density environments are populated only by galaxies and QGs with stellar mass lower than $\sim 10^{10.5}\,M_{\odot}$. Vice versa, galaxies and QGs with the highest masses reside only in high-density environments.

We divide the sample into three environmental classes, separated at $\rho_{\rm env} = 22.45$ and $\rho_{\rm env} = 62.87$, respectively, which are defined basing on the tertiles of the $\rho_{\rm env}$ distribution of the parent SF-Alldet population. We define 'low-D' those galaxies belonging to the first tertile; 'interm-D' those in the second tertile and 'high-D' those galaxies belonging to the third tertile. We compare the environment of the QG candidates against that of the parent SF population, finding a hint of a lack of QGs in low-D environment and an excess in high-D environment, at high significance level ($\sim 3\sigma$) only for QGs-B (see Fig. 20). Indeed, a KS test confirms this behaviour at a significance level $\alpha = 0.05$ only for QGs-B, while QG-A and SF-Alldet populations appear to have a compatible $\rho_{\rm env}$.

In Table 5 we compare also the fraction in the three different environments of the QG candidates against other two reference samples of no-H α and SF-[O III]undet galaxies. As it is possible to note, SF-OIIIundet galaxies are even more extreme than QGs-B, given that the 57.6 $\pm$0.6 per cent of them in the high-D tertile, and reside at each mass in environments which are intermediate between SF and no-H α galaxies.

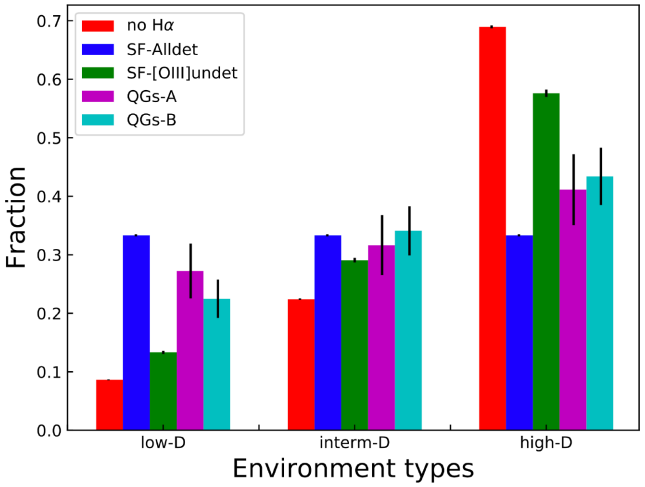

Figure 20. Distribution of no-Hα (red), SF-Alldet (blue), SF-[O III]undet (green), QGs-A (magenta), and QGs-B (cyan) in three environment types (i.e. low-D, interm-D, high-D).

We also analyse the Richness (R) and the 'Brightness Rank' (hereafter BR) to evaluate whether the candidates are either the dominant/brightest galaxies or satellites within their group/cluster. BR ranges from the values of the group/cluster richness R to 1. In particular, BR=richness and BR=1 indicate that the considered galaxy is the faintest or the brightest (and thus the most massive) in its group/cluster, respectively. We define as 'central' a galaxy whose brightness rank is equal to 1.

Fig. 21 shows $\rho_{\rm env}$ as a function of BR of the galaxies in their own environment. We find (see Fig. 21) that the bulk of QGs in high-D enviroments are satellites (76.9 per cent and 63.4 per cent, respectively, for QGs-A and -B), with percentages higher than those of the parent SF-Alldet population (57.3 per cent) and of the SF-OIIIundet population (46.1 per cent). Finally, almost all (>90 per cent) galaxies belonging to groups/clusters including more than 30 members ($R > 30$) are in high-D environment and all the QGs in these extreme dense environments (i.e. 5.70 $\pm$ 1.95 per cent of QGs-A and 4.65 $\pm$ 1.37 per cent of QGs-B) are satellites.

Therefore, we conclude that our QGs are preferentially satellite galaxies within groups of medium and high densities, showing an excess in high-density environments compared to SF galaxies.

5 DISCUSSION

5.1 Quenching time-scale

In this section, we use the fraction of our selected QGs to estimate the time-scale of the star-formation quenching, as suggested by C17. We define $t_{\rm Q}$ as the time elapsed from when the candidate was a typical star-forming galaxy to the moment in which it is observed. For QGs-A, this happens when our tracer of the ionization parameter (i.e. [O III]/H α) becomes 3σ lower (i.e. about 0.4 dex) than the median of the [O III]/H α distribution of SF galaxies. For QGs-B this occurs instead when [O III]/[N II] becomes 3σ lower than the [O III]/[N II] expected from its estimated metallicities.

First, we derive the fraction of the QGs-A and QGs-B as the number of QGs over the number (i.e. 174000) of SF galaxies (SF-Alldet plus SF-[O III]undet). We obtain a fraction of 0.11 per cent and 0.18 per cent, for the QGs-A and QG-B, respectively. To obtain the observed quenching time-scale of our QGs, following C17, we

Table 5. The environment of the quenching candidates with methods A and B compared against three control samples: SF-Alldet, SF-[O III]undet (the subsample in which the candidates are selected), and no-H α. The column Global lists the ratio between the number of objects in common with the Tempel et al. (2014) sample over the total number in each sub-sample.

	Global	Low-D ($\rho_{env.} < 22.45$)	Interm-D ($22.45 \leq \rho_{env.} < 62.87$)	High-D ($\rho_{env.} \geq 62.87$)
QGs-A	158/192	27.2 ± 4.7 per cent	31.7 ± 5.1 per cent	41.1 ± 6.1 per cent
QGs-B	258/308	22.5 ± 3.3 per cent	34.1 ± 4.2 per cent	43.4 ± 4.9 per cent
SF-Alldet	130651/148145	33.3 ± 0.2 per cent	33.3 ± 0.2 per cent	33.3 ± 0.2 per cent
SF-[O III]undet	22667/25911	13.3 ± 0.3 per cent	29.1 ± 0.4 per cent	57.6 ± 0.6 per cent
no-H α	174741/201527	8.6 ± 0.1 per cent	22.4 ± 0.1 per cent	69.0 ± 0.3 per cent

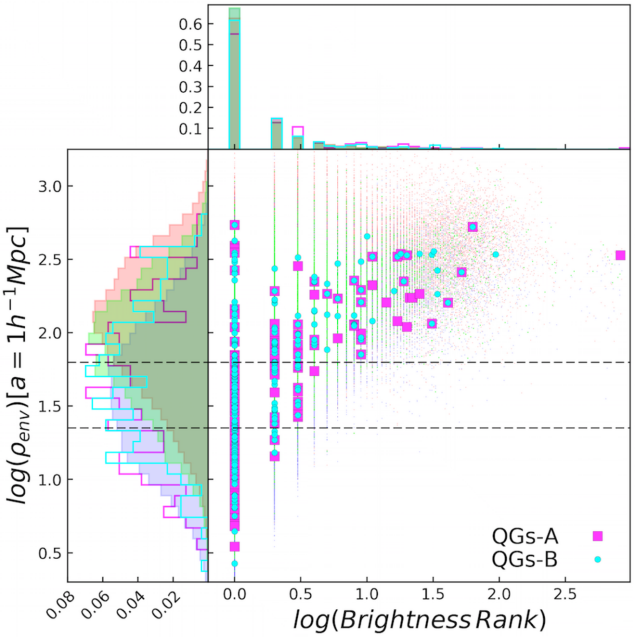

Figure 21. Normalized environmental density of galaxies ρ_{env} (smoothing scales of $1\,h^{-1}$ Mpc) versus the brightness rank. The two dashed lines (at $\rho_{env} = 22.45$ and $\rho_{env} = 62.87$, respectively) divide the SF-Alldet ρ_{env} distribution into three tertiles.

multiply this fraction (F_{QGs}) by the typical lifetime of an SF galaxy, that could be represented by the doubling mass time $t_{doubling}$ [i.e. the time needed to a galaxy for doubling its stellar mass ($\sim$1/sSFR; e.g.) Guzmán et al. 1997; Madau & Dickinson 2014]:

$$t_Q = F_{QGs} \times t_{doubling} = F_{QGs} \times \frac{1}{\mathrm{sSFR}} \quad (6)$$

Following the empirical relations by Karim et al. (2011), we derive the quantity 1/sSFR, which amounts to $\sim$8.8 and $\sim$10 Gyr for QGs-A and -B, respectively (assuming a median mass $\log(M/M_\odot) \simeq 10.1$ and 10.4 for QGs-A and -B, respectively). Then we obtain $t_Q \sim$ 9.7−18 Myr. This t_Q is a lower limit because of the several conservative assumptions taken into account for the selection of the candidates and because the flux limit of the survey allows to select only the most extreme candidates.

We derive also an upper limit to t_Q by assuming that about 50 per cent of SF-[O III]undet population (i.e. $\sim$13000 galaxies) is in a low ionization state. This is supported by the fact that the [O III]/Hα ratio in their median stacked spectrum (see Fig. 6) is 1σ below the median value of SF galaxies (therefore at least 50 per cent of SF-[O III]undet are above 1σ value of SF galaxies, i.e. are consistent to be SF galaxies). In this case, the observed fraction of SF-[O III]undet is $\sim$7.5 per cent and, with a median $\log(M/M_\odot) \sim 10.6$ (i.e. 1/sSFR $\sim$10.1 Gyr, following Karim et al. 2011), the t_Q is $\sim$0.76 Gyr, compatible with galaxies which are experiencing a smoother and slower quenching.

Finally, we perform a survival analysis (ASURV, i.e. Kaplan–Meier estimator) of the distribution of [O III]/Hα in slices of [N II]/[O II]. We find that 938 (i.e. a fraction of 0.58 per cent) among [O III]undet galaxies are re-distributed below 3σ (i.e. the thresholds for QGs-A), representing therefore the global fraction of QGs-A and leading to a quenching time-scale of $\hat{t}_Q \sim 50$ Myr. This time $\hat{t}_Q$ should represent a good statistical measurement of the true quenching time-scale for the adopted threshold. With the same ASURV analysis we confirm the consistency of the assumption that about 50 per cent of [O III]undet galaxies are re-distributed below 1σ, accordingly to the value obtained from the median-stacked spectra.

We, therefore, convert these values of t_Qs in an e-folding time τ_Q for the star formation quenching history. Adopting the C17 models, we derive the relation between the time needed by the [O III/Hα] ratio to decrease by 0.42 dex and τ_Q. We find that our lower limit time-scales are compatible with an exponential $\tau_Q \simeq$ 18−34 Myr for QGs-A and -B respectively. Instead, from a linear extrapolation at $t_Q \sim 0.76$ Gyr we obtain a $\tau_Q \sim 1.5$ Gyr for the upper limit time-scale. Finally, from $\hat{t}_Q$ we obtain an estimate of $\hat{\tau}_Q \sim 90$ Myr.

In summary, from the fraction of our QGs candidates, we derive a broad range of quenching time-scales of 10 Myr $< t_Q <$ 0.76 Gyr, and a statistically estimate of $\hat{t}_Q \sim 50$ Myr for QGs-A. These values correspond to a range for the e-folding time-scale of the star formation quenching history of 18 Myr $< \tau_Q <$ 1.5 Gyr and an estimate of $\hat{\tau}_Q \sim 90$ Myr.

5.2 Quenching mechanisms

Our sample of QG candidates is fundamental to get insights on the physical mechanisms driving the quenching of their SF. From our sample, we find a relatively rapid time-scale for quenching (from few Myr to at most 1.5 Gyr) acting in galaxies with $\log(M/M_\odot) > 9.5$, being preferentially satellites in intermediate to high-density environments, and having their morphology almost unaffected. A smaller fraction ($\sim$25 per cent) of our QGs is, however, also in low-density environments, and likely isolated. Only a small fraction (12−17 per cent) of them have already a compact morphology consistent with a morphological transformation. Therefore, different mechanisms should have driven their quenching, in particular in isolated and high-D environments, and in different evolutionary epochs.

In general, the SFR in the inner SF regions of main-sequence galaxies is thought to be fueled through a continuous replenishment of low-metallicity and relatively low-angular momentum gas from the surrounding hot corona (Pezzulli & Fraternali 2016), regulated via stellar feedback (e.g. galactic fountain accretion;

Shapiro & Field 1976; Fraternali & Binney 2006) until a quenching mechanism shall act to break the process. Recently, Armillotta, Fraternali & Marinacci (2016) found that the efficiency of fountain-driven condensation is strictly dependent on the coronae temperature. In coronae with temperatures higher than 4×10^6K, the process is highly inefficient. Hence, isolated QG candidates which are more massive than the Milky Way could have lost the ability to cool coronae gas and, after the consumption of their gas reservoir, they could start to quench the star formation. Instead, in isolated QGs less massive than the Milky Way, strong stellar feedback (i.e. SN and strong stellar wind) may have inhibited the accretion of cold gas from the corona (Veilleux, Cecil & Bland-Hawthorn 2005; Sokołowska et al. 2016).

In denser environments there are several quenching mechanisms which can affect our satellite QGs. However, the most likely process should leave the morphology almost unaffected. In dense environment, in which the velocity of galaxies may be sufficiently high, the ram pressure could remove cold gas from the reservoir of the satellite galaxies (e.g. Gunn & Gott 1972; Quilis, Moore & Bower 2000; Poggianti et al. 2004; Kawinwanichakij et al. 2017; Papovich et al. 2018). This 'ram pressure stripping' results in a quenching of the star formation, with a relatively short time-scale (∼200 Myr–≥1Gyr, e.g. Steinhauser, Schindler & Springel 2016). However, there is general consensus that 'strangulation' (or 'starvation') is the dominant quenching mechanism in satellite galaxies (e.g. Treu et al. 2003; van den Bosch et al. 2008; Peng et al. 2015). When the corona of a galaxy interacts hydrodynamically with the hot and dense intra-cluster medium of a larger halo, its hot and diffuse gas could be stripped (e.g. Larson et al. 1980; Balogh et al. 2000). This effect leads to a suppression of the accretion on to the disc, thus resulting in a gradual decline of the SFR until the exhaustion of the gas reservoir of the galaxy. Peng et al. (2015) claimed that the primary quenching mechanism for galaxies is the strangulation. They derive the quenching time-scale due to this mechanism as the gas depletion time needed to explain the differences in metallicity between the SF population and the quiescent one, finding that models of 4 Gyr are the most suitable for this task (see also Maier et al. 2016). We compare this time-scale with the estimate of the time (t_P) needed by a galaxy to decrease its sSFR from typical main sequence values (i.e. ∼−10 in log-scale for $\log(M/M_\odot) \sim 10.4$; e.g. Karim et al. 2011) to the typical sSFR of the passive population. (i.e. ∼−11 in log scale; e.g. Pozzetti et al. 2010; Ilbert et al. 2013). For the *e*-folding time τ_Q we derive a lower limit time-scale t_P of ∼40–80 Myr and an upper limit of ∼3.5 Gyr.

Recently, it is gaining consensus a scenario (i.e. 'Delayed then rapid' quenching; Wetzel et al. 2013; Fossati et al. 2017) in which the quenching of satellites in dense environments has been proposed to be divided into two phases: a relatively long period ('the delay time') in which the star formation does not differ strongly from the main-sequence values (2–4Gyrafter first infall), followed by a phase in which the SFR drops rapidly ('the fading time') with an exponential fading with an e-*folding* time of 0.2–0.8 Gyr (lower for more massive galaxies) that is independent on host halo mass.

About 70 per cent and 80 per cent of QGs-A and -B reside in high- and intermediate-density environments and the vast majority of them are satellites. Hence, the derived τ_Q for our QGs allow to perform a direct comparison with the quenching time-scales in Wetzel et al. (2013). Although the range derived for τ_Q is quite broad, we can at least confirm that our time-scales are compatible with theirs.

We can also make a further comparison with the Wetzel et al. (2013) predictions by using the median L(H α) of the stacked spectra (see Section 4.1) as a proxy of the median SFR, and comparing them to the value of the SF galaxy sample (0.8 for QGs-A and 0.9 for QGs-B). Assuming that, after the start of the quenching, the SFR of an SF galaxy decreases to the value of $SFR_{QGs}(t_Q)$, we can estimate the exponential *e*-folding time, deriving $\tau_Q \sim$ 50–190 Myr for the median QGs-A and -B spectra that are closer to those found by Wetzel et al. (2013).

It is also interesting to limit the discussion to the central quenching galaxies. There is consensus that the quenching is slower for central galaxies (e.g. Hahn, Tinker & Wetzel 2017). Focusing on central galaxies in high-density environment, we found a lower limit t_Q of 8.8−20 Myr, respectively, for central QGs-A and -B and an upper limit $t_Q \sim 1.4$ Gyr. These time-scales are compatible with lower limit exponential e-folding τ_Q of 16−38 Myr and an upper limit $\tau_Q \sim 2.8$ Gyr. Following an approach similar to that of Wetzel et al. (2013), Hahn et al. (2017) found that central galaxies quench the star formation with an *e*-folding time between 0.5 and 1.5 Gyr (lower for massive galaxies) and also in this case we are compatible with their result.

There is general consensus that environmental mechanisms take longer time (2−3Gyr; e.g. Balogh et al. 2000; Wang et al. 2007) to start to affect the SFR of satellites. Hence, this should be the most probably scenario also for our satellites before the starting of the quenching. Moreover, we found that our quenching time-scales are compatible with an exponential decrement like that of Wetzel et al. (2013), although without an overwhelming. We can conclude that the properties of our QG candidates can be preferentially explained by a 'Delayed then rapid' quenching of satellites galaxies, due to the final phase of an environmental quenching mechanism(s).

Strangulation, ram-pressure stripping, and harassment (e.g. Farouki & Shapiro 1981) are the most important mechanisms that act on satellites leading to the quenching of their star formation. Since we can safely exclude from a visual inspection that any of our candidates are experimenting harassment, the natural conclusion for our QGs that reside in high- and intermediate-density environment is that strangulation and ram-pressure stripping should play a primary role in the halt of the star formation. However, different mechanisms can also work together to quench the star formation in galaxies. Moreover, even if our methods are not sensitive to AGN feedback (e.g. De Lucia et al. 2006; Fabian 2012; Cimatti et al. 2013; Cicone et al. 2014) as quenching mechanism, due to our a priori exclusion of AGNs, we cannot exclude that an early AGN phase could be responsable and could have quenched our QGs. In this case, the AGN phase should have finished before the quenching of the star formation. On the other end, it is important to remind that other authors predict the formation of ETGs without invoking the AGN feedback (e.g. Naab, Khochfar & Burkert 2006; Johansson, Naab & Ostriker 2012).

Finally, we stress that our QGs still have an ionized-gas phase, as witnessed by their H α emission, even if weaker than in the parent sample of SF galaxies, suggesting that gas depletion is indeed ongoing. In the future, after the disappearance of late-B stars and the consequently disappearance of hard-UV photons, this gas could be cooled down being available for a new phase of star formation. However, if we are witnessing a minimum in the SFH of our quenching candidates, we should observe QGs at all masses, also lower than $10^{9.5}$ $M_\odot$ (i.e. the less-massive QG in our sample). To confirm the final passive fate of our QGs, connected to the presence or absence of residual gas and, at the same times explaining the observed H α emission, more observations are needed and in particular we need to study the cold gas phase distribution from ALMA observations (see, for instance, Decarli et al. 2016; Lin et al. 2017).

6 SUMMARY

In this work, we analyse a sample of ∼174000 SDSS-DR8 SF galaxies at $0.04 \leq z < 0.21$ to provide for the first time a sample of quenching galaxy (QGs) candidates selected just after the interruption of their star formation.

We follow the approach introduced by C17 to select QG candidates on the basis of emission line flux ratios of higher-to-lower ionization lines (i.e. [O III]/H α) which are sensitive to the ionization level. The main issue of this approach is that the [O III]/Hα ratio is affected by an ionization-metallicity degeneracy.

In order to mitigate this degeneracy, we set up two different methods:

(i) *Method A*: following C17, we exploit the plane [O III] /H α versus [N II]/[O II] to select galaxies with the lowest [O III] /H α values for a given metallicity (i.e. using [N II]/[O II] as metallicity indicator). By analysing the statistical distribution of our samples, we identify an excess of galaxies consistent with being a population separated from the SF sample, having intrinsically lower [O III]/Hα values, and hence lower ionization levels. This method is demonstrated to be stable against the choice of the dust attenuation law. We also tested an alternative diagram involving [O III]/Hβ versus [N II]/[S II], which has the advantage of being less affected by dust extinction, although it involves weaker lines.

(ii) *Method B*: an alternative method to mitigate the metallicity degeneracy is to select galaxies for which the [O III] flux is weaker than the minimum value expected from their metallicity, exploiting the two relations [N II]/[O II] versus 12+log(O/H) and 12+log(O/H) versus [O III]/[N II].

Applying these methods, we select two samples of QG candidates and analyse their main properties. Our results can be summarized as follows:

(i) We select 192 candidates (QGs-A) and 308 candidates (QGs-B), using Methods A and B, respectively. There is an intersection of 120 QGs between them, and the QGs out of the intersection are close to the threshold criterion of both methods. QGs-B show, on average, higher values of [N II] /H α and of [N II]/[O II] compared to QGs-A, suggesting that they have a statistically higher metallicity than QGs-A.

(ii) The median stacked spectra, corrected for dust extinction, of QGs-A and QGs-B have a blue stellar continuum, suggesting a young mean stellar population. The analysis confirms a weak [O III] emission and that also other high ionization emission lines (such as [Ne III]) are weak in both QGs stacked spectra, and the [O III] /H α ratios are consistent with a low ionization level. On the contrary, [O II], H α and H β (i.e. low ionization lines) are still strong and with an Hα flux slightly weaker (∼80 per cent) than the one of SF galaxies.

(iii) We find that QGs have D_n4000 and EW(H α) values intermediate between SF and already quenched galaxies, confirming that they have just stopped their star formation and have a young/intermediate mean stellar population.

(iv) In the colour-mass diagram, the bulk of the QGs-A and QGs-B resides in the blue cloud region, and only few of them (∼3 per cent) lie in the green valley region. The QGs have masses $\log(M/M_\odot) > 9.5$, comparable with those of the SF population, being the QGs-B, on average, more massive. This suggests that, as expected in a downsizing scenario, star formation quenching has not started yet for low-mass galaxies, consistently with a lack of low-mass red galaxies. Their H α emission is compatible with a just quenched SFR of the order of 0.6–10 $M_\odot$ yr^{-1}, similar to that of the SF main sequence population, suggesting the presence of residual ionized gas in our QGs. The emission from the median stacked spectra is, however, weaker than that in the SF population, suggesting that the depletion of the gas has started.

(v) The morphology and concentration index (C=R90/R50) of QGs are similar to those of the SF population, suggesting that no morphological transformation has occurred yet, in the early phase after the quenching of the star formation. However, some of them have a concentration index higher than the threshold that divides the early-type from the other galaxy types (i.e. $C > 2.6$) and they could have experienced morphological transformation during the interruption of the star formation.

(vi) Compared to the parent SF population, we find an excess of QGs in high-density environments (∼42 per cent), in particular for QGs-B. QGs in high-density environments are preferentially satellites (from ∼60 to 80 per cent). Approximatively 5 per cent of QGs are in groups/clusters which have more than 30 members, but no one of them is the brightest galaxy in its environments.

(vii) From the fraction of QG candidates (∼0.11 − 0.18 per cent of the SF population) we estimate the quenching time-scales for these populations to be between 10 and 18 Myr. These values are compatible with the sharp quenching models by C17. If we assume that at most 50 per cent the entire SF-[O III]undet population (∼7.5 per cent) is in a low ionization state, as witnessed by the low but not extreme [O III] /H α ratio in their stacked spectrum, we obtain an upper limit to the quenching time-scale of $\simeq 0.76$ Gyr. In this case, the quenching time-scale is compatible with galaxies which are experiencing a more smoothed and slower quenching (C17). We convert this range into an e-folding time-scale for the SFR quenching history, finding 18 Myr $< \tau_Q <$ 1.5 Gyr.

(viii) From a survival analysis we find that 938 (∼0.58 per cent) among SF-[O III]undet galaxies are consistent to be QGs candidates. We, therefore, derive a statistical measurement of the quenching time-scale $\hat{\tau}_Q$ of ∼50 Myr and $\hat{\tau}_Q \sim 90$ Myr.

This analysis, based on a new spectroscopic approach, leads to the identification of a population of galaxy candidates selected right after the quenching. Most of our QGs would not have been selected as an intermediate population using colour criteria, or in the SFR-mass plane.

We conclude that these galaxies, which are quenching their star formation on a short time-scale (from few Myr to less than 1 Gyr), preferentially reside in intermediate- to high-density environments, are satellites and have not morphologically transformed into spheroidal red passive galaxies yet. All these properties could be explained by a 'Delayed then rapid' (see Wetzel et al. 2013) quenching scenario in satellites galaxies, due to the final phase of strangulation or ram pressure stripping.

However, to confirm the proposed scenario and the presence or absence of a reservoir of gas, more observations are needed. For example, cold gas phase distribution could be derived from ALMA observations (e.g. Decarli et al. 2016; Lin et al. 2017), while the spatial distribution of quenching can be analysed using integral field unit (IFU) spectroscopic data to get insights about the inside-out scenario (e.g. the MANGA public survey, Bundy et al. 2015; the SAMI galaxy survey, Green et al. 2018; the MUSE-VLT data Bacon et al. 2010 and, in the future, WEAVE-IFU data, Dalton et al. 2014).

ACKNOWLEDGEMENTS

The authors thank the anonymous referee for helpful suggestions and very constructive comments. We are grateful to Filippo Frater-

nali, Paola Popesso, Gianni Zamorani, Roberto Maiolino, Christian Maier, Filippo Mannucci, Sirio Belli, and Alice Concas for useful discussion and suggestions and Cristian Vignali to help us for the ASURV analysis. The authors also acknowledge the grants ASI n.I/023/12/0 'Attività relative alla fase B2/C per la missione Euclid' and PRIN MIUR 2015 'Cosmology and Fundamental Physics: illuminating the Dark Universe with Euclid'. Funding for the SDSS and SDSS-II has been provided by the Alfred P. Sloan Foundation, the Participating Institutions, the National Science Foundation, the U.S. Department of Energy, the National Aeronautics and Space Administration, the Japanese Mon-bukagakusho, the Max Planck Society, and the Higher Education Funding Council for England. The SDSS web site is http://www.sdss.org/. The SDSS is managed by the Astrophysical Research Consortium for the Participating In stitutions. The Participating Institutions are the American Museum of Natural History, Astrophysical Institute Pots-dam, University of Basel, University of Cambridge, Case Western Reserve University, University of Chicago, Drexel University, Fermilab, the Institute for Advanced Study, the Japan Participation Group, Johns Hopkins University, the Joint Institute for Nuclear Astrophysics, the Kavli Institute for Particle Astrophysics and Cosmology, the Korean Scientist Group, the Chinese Academy of Sciences (LAMOST), Los Alamos National Laboratory, the Max-Planck-Institute for Astronomy (MPIA), the Max-Planck-Institute for Astrophysics (MPA), New Mexico State University, Ohio State University, University of Pittsburgh, University of Portsmouth, Princeton University, the United States Naval Observatory, and the University of Washington.

REFERENCES

Aihara H. et al., 2011, ApJS, 193, 29
Armillotta L., Fraternali F., Marinacci F., 2016, MNRAS, 462, 4157
Bacon R. et al., 2010, in McLean I. S., Ramsay S. K., Takami H., eds, Proc. SPIE 7735, Ground-based and Airborne Instrumentation for Astronomy III. SPIE, San Diego, p. 773508
Baldry I. K., Glazebrook K., Brinkmann J., Ivezić Ž., Lupton R. H., Nichol R. C., Szalay A. S., 2004, ApJ, 600, 681
Baldwin J. A., Phillips M. M., Terlevich R., 1981, PASP, 93, 5 (BPT)
Balogh M. L., Morris S. L., Yee H. K. C., Carlberg R. G., Ellingson E., 1999, ApJ, 527, 54
Balogh M. L., Navarro J. F., Morris S. L., 2000, ApJ, 540, 113
Balogh M. L., Baldry I. K., Nichol R., Miller C., Bower R., Glazebrook K., 2004, ApJ, 615, L101
Baron D., Netzer H., Poznanski D., Prochaska J. X., Förster S., Natascha M., 2017, MNRAS, 470, 1687
Bekki K., 2009, MNRAS, 399, 2221
Belfiore F. et al., 2017, MNRAS, 466, 2570
Bell E. F. et al., 2004, ApJ, 608, 752
Bell E. F. et al., 2012, ApJ, 753, 167
Blanton M. R., 2006, ApJ, 648, 268
Blanton M. R. et al., 2003, ApJ, 594, 186
Brammer G. B. et al., 2009, ApJ, 706, L173
Brinchmann J., Charlot S., White S. D. M., Tremonti C., Kauffmann G., Heckman T., Brinkmann J., 2004, MNRAS, 351, 1151
Bruzual G., Charlot S., 2003, MNRAS, 344, 1000
Bundy K. et al., 2006, ApJ, 651, 120
Bundy K. et al., 2015, ApJ, 798, 7
Calzetti D., Armus L., Bohlin R. C., Kinney A. L., Koornneef J., Storchi-Bergmann T., 2000, ApJ, 533, 682
Cappellari M., Emsellem E., 2004, PASP, 116, 138
Cassata P. et al., 2008, A&A, 483, L39
Charlot S., Longhetti M., 2001, MNRAS, 323, 887
Cicone C. et al., 2014, A&A, 562, A21
Cimatti A. et al., 2013, ApJ, 779, L13
Cirasuolo M. et al., 2007, MNRAS, 380, 585
Citro A., Pozzetti L., Moresco M., Cimatti A., 2016, A&A, 592, A19
Citro A., Pozzetti L., Quai S., Moresco M., Vallini L., Cimatti A., 2017, MNRAS, 469, 3108 (C17)
Conroy C., van Dokkum P. G., 2016, ApJ, 827, 9
Cucciati O. et al., 2006, A&A, 458, 39
Dalton G. et al., 2014, in Ramsay S. K., McLean I. S., Takami H., eds, Proc. SPIE 9147, Ground-based and Airborne Instrumentation for Astronomy V. SPIE, Montréal, p. 91470L
De Lucia G., Springel V., White S. D. M., Croton D., Kauffmann G., 2006, MNRAS, 366, 499
Decarli R. et al., 2016, ApJ, 833, 69
Dekel A., Birnboim Y., 2008, MNRAS, 383, 119
Faber S. M. et al., 2007, ApJ, 665, 265
Fabian A. C., 2012, ARA&A, 50, 455
Farouki R., Shapiro S. L., 1981, ApJ, 243, 32
Fossati M. et al., 2017, ApJ, 835, 153
Fraternali F., Binney J. J., 2006, MNRAS, 366, 449
Gilbank D. G., Baldry I. K., Balogh M. L., Glazebrook K., Bower R. G., 2010, MNRAS, 405, 2594
Goto T., 2005, MNRAS, 357, 937
Goto T., Yamauchi C., Fujita Y., Okamura S., Sekiguchi M., Smail I., Bernardi M., Gomez P. L., 2003, MNRAS, 346, 601
Green A. W. et al., 2018, MNRAS, 475, 716
Gunn J. E., Gott III J. R., 1972, ApJ, 176, 1
Guzmán R., Gallego J., Koo D. C., Phillips A. C., Lowenthal J. D., Faber S. M., Illingworth G. D., Vogt N. P., 1997, ApJ, 489, 559
Hahn C., Tinker J. L., Wetzel A., 2017, ApJ, 841, 6
Hogg D. W. et al., 2003, ApJ, 585, L5
Holden B. P., van der Wel A., Rix H.-W., Franx M., 2012, ApJ, 749, 96
Hopkins A. M. et al., 2003, ApJ, 599, 971
Hubble E. P., 1926, ApJ, 64
Huertas-Company M., Aguerri J. A. L., Bernardi M., Mei S., Sánchez Almeida J., 2011, A&A, 525, A157
Ilbert O. et al., 2013, A&A, 556, A55
Johansson P. H., Naab T., Ostriker J. P., 2012, ApJ, 754, 115
Juneau S. et al., 2014, ApJ, 788, 88
Karim A. et al., 2011, ApJ, 730, 61
Kauffmann G. et al., 2003, MNRAS, 346, 1055
Kaviraj S., 2010, MNRAS, 408, 170
Kawinwanichakij L. et al., 2017, Apj, 847, 134
Kennicutt R. C., Jr, 1998, ARA&A, 36, 189
Kewley L. J., Dopita M. A., Sutherland R. S., Heisler C. A., Trevena J., 2001, ApJ, 556, 121
Kewley L. J., Jansen R. A., Geller M. J., 2005, PASP, 117, 227
Kriek M., van der Wel A., van Dokkum P. G., Franx M., Illingworth G. D., 2008, ApJ, 682, 896
Kroupa P., 2001, MNRAS, 322, 231
Larson R. B., Tinsley B. M., Caldwell C. N., 1980, ApJ, 237, 692
Levesque E. M., Leitherer C., 2013, ApJ, 779, 170
Lin L. et al., 2017, ApJ, 851, 18
Madau P., Dickinson M., 2014, ARA&A, 52, 415
Maier C. et al., 2016, A&A, 590, A108
Martig M., Bournaud F., Teyssier R., Dekel A., 2009, ApJ, 707, 250
Martin D. C. et al., 2007, ApJS, 173, 342
McIntosh D. H. et al., 2014, MNRAS, 442, 533
Mendel J. T., Simard L., Ellison S. L., Patton D. R., 2013, MNRAS, 429, 2212
Mendez A. J., Coil A. L., Lotz J., Salim S., Moustakas J., Simard L., 2011, ApJ, 736, 110
Moore B., Governato F., Quinn T., Stadel J., Lake G., 1998, ApJ, 499, L5
Moresco M. et al., 2012, J. Cosmol. Astropart. Phys., 8, 006
Mortlock A., Conselice C. J., Bluck A. F. L., Bauer A. E., Grützbauch R., Buitrago F., Ownsworth J., 2011, MNRAS, 413, 2845
Moustakas J. et al., 2013, ApJ, 767, 50
Muzzin A. et al., 2013, ApJS, 206, 8
Naab T., Khochfar S., Burkert A., 2006, ApJ, 636, L81
Nagao T., Maiolino R., Marconi A., 2006, A&A, 459, 85

Osterbrock D. E., 1989, Astrophysics of Gaseous Nebulae and Active Galactic Nuclei. University Science Book, Mill Valley, CA
Papovich C. et al., 2018, ApJ, 854, 30
Peng Y., Maiolino R., Cochrane R., 2015, Nature, 521, 192
Peng Y.-j. et al., 2010, ApJ, 721, 193
Peng Y.-j., Lilly S. J., Renzini A., Carollo M., 2012, ApJ, 757, 4
Pezzulli G., Fraternali F., 2016, MNRAS, 455, 2308
Poggianti B. M., Bridges T. J., Komiyama Y., Yagi M., Carter D., Mobasher B., Okamura S., Kashikawa N., 2004, ApJ, 601, 197
Poggianti B. M. et al., 2008, ApJ, 684, 888
Pozzetti L. et al., 2010, A&A, 523, A13
Quilis V., Moore B., Bower R., 2000, Science, 288, 1617
Quintero A. D. et al., 2004, ApJ, 602, 190
Rodighiero G. et al., 2011, ApJ, 739, L40
Salim S., 2014, Serb. Astron. J., 189, 1
Salim S. et al., 2007, ApJS, 173, 267
Salim S. et al., 2009, ApJ, 700, 161
Sarzi M. et al., 2006, MNRAS, 366, 1151
Schawinski K. et al., 2010, ApJ, 711, 284
Schawinski K. et al., 2014, MNRAS, 440, 889
Schiminovich D. et al., 2007, ApJS, 173, 315
Seaton M., 1979, MNRAS, 187, 73
Shapiro P. R., Field G. B., 1976, ApJ, 205, 762
Smethurst R. J. et al., 2016, MNRAS, 463, 2986
Sokołowska A., Mayer L., Babul A., Madau P., Shen S., 2016, ApJ, 819, 21
Somerville R. S., Davé R., 2015, ARA&A, 53, 51
Steinhauser D., Schindler S., Springel V., 2016, A&A, 591, A51
Strateva I. et al., 2001, AJ, 122, 1861
Strauss M. A. et al., 2002, AJ, 124, 1810
Tacchella S. et al., 2015, Science, 348, 314
Tempel E. et al., 2014, A&A, 566, A1
Thomas D., Maraston C., Schawinski K., Sarzi M., Silk J., 2010, MNRAS, 404, 1775
Tremonti C. A. et al., 2004, ApJ, 613, 898
Treu T., Ellis R. S., Kneib J.-P., Dressler A., Smail I., Czoske O., Oemler A., Natarajan P., 2003, ApJ, 591, 53
van den Bosch F. C., Aquino D., Yang X., Mo H. J., Pasquali A., McIntosh D. H., Weinmann S. M., Kang X., 2008, MNRAS, 387, 79
Veilleux S., Cecil G., Bland-Hawthorn J., 2005, ARA&A, 43, 769
Wang L., Li C., Kauffmann G., De Lucia G., 2007, MNRAS, 377, 1419
Wetzel A. R., Tinker J. L., Conroy C., van den Bosch F. C., 2013, MNRAS, 432, 336
Williams R. J., Quadri R. F., Franx M., van Dokkum P., Labbé I., 2009, ApJ, 691, 1879
Willmer C. N. A. et al., 2006, ApJ, 647, 853
Wyder T. K. et al., 2007, ApJS, 173, 293
York D. G. et al., 2000, AJ, 120, 1579

APPENDIX A: FIBRE APERTURE EFFECTS

As mentioned in Section 2.1, we select galaxies at $z > 0.04$, following the prescription of Kewley et al. (2005), in order to avoid strong fibre aperture effects on SFRs, extinction, and metallicity. Indeed, we stress that our analysis is limited to the area of galaxies covered by the fibre. With the adopted cosmology, at $z = 0.04$ and $z = 0.21$, the SDSS fibre radius (1.5 arcsec) corresponds to ∼1.2 and ∼5.2 kpc, respectively. In Fig. A1 we show the size-redshift relation for our sample. The size is represented by the R50 radius. Roughly all the candidates have R50 larger than the fibre radius. Therefore, we can analyse the quenching only in the inner part of our QG candidates. In order to test whether we could extend our results to the whole galaxy, we explore the impact of the aperture on the ionization indicator [O III]/H α. Fig. A2 shows the [O III]/H α as a function of the fraction of flux inside the fibre (u-band) with respect to the total u-band flux (u-band Petrosian flux; Strauss et al. 2002). There is no evident trend, with QGs candidates distributed over the whole range, even at the lowest ionization levels ($\log([\mathrm{O\,III}]/\mathrm{H}\,\alpha) < -1.3$). This test suggests that, in this redshift range, the fibre aperture does not affect significantly our analysis, even if our results are clearly relative only to the region included in the fibre.

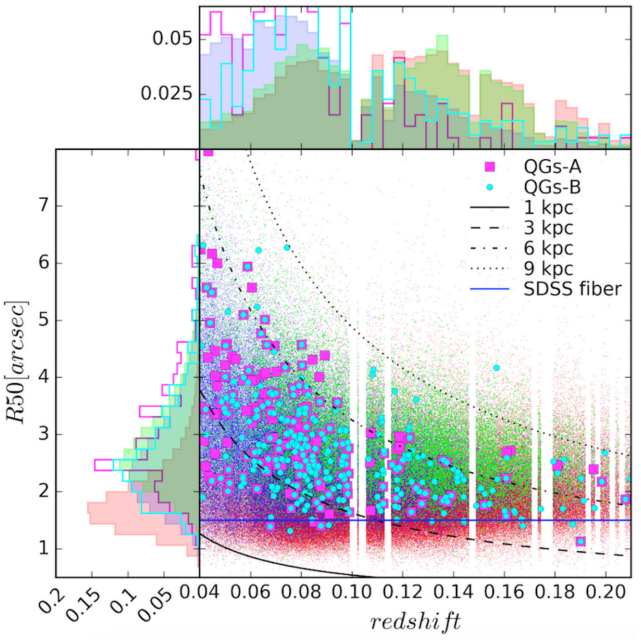

Figure A1. The size-redshift relation for our sample and quenching candidates. The horizontal blue line represents the radius of the SDSS fibre aperture, while the black curves represent the kpc/arcsec relations obtained from the adopted cosmology.

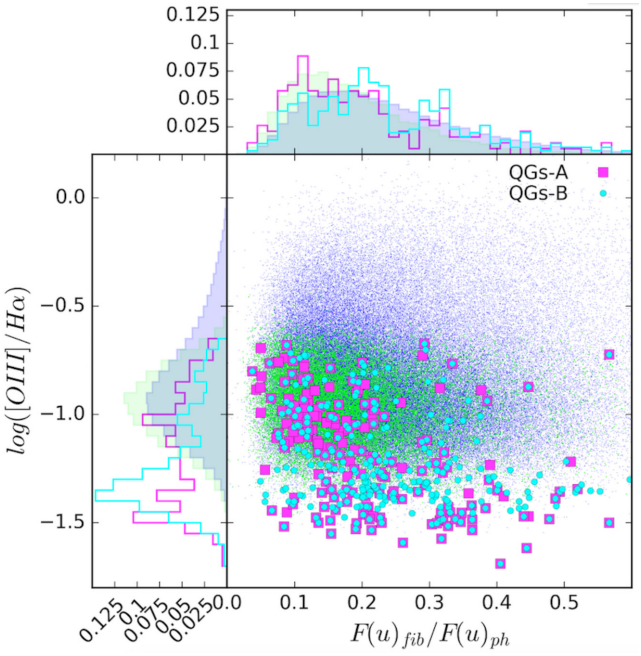

Figure A2. [O III]/H α as a function of the ratio between the u-band flux inside the fibre and total. The colour code is the same of Fig. 8.

This paper has been typeset from a TEX/LATEX file prepared by the author.